

Per Henning Hammerstad Møllevold

Voltage distribution in medium voltage machines for aerospace applications fed by power converters

Master's thesis in Energy and Environmental Engineering

Supervisor: Pål Keim Olsen

Co-supervisor: Njål Rotevatn and Viljar Fjellanger

June 2022

Per Henning Hammerstad Møllevold

Voltage distribution in medium voltage machines for aerospace applications fed by power converters

Master's thesis in Energy and Environmental Engineering
Supervisor: Pål Keim Olsen
Co-supervisor: Njål Rotevatn and Viljar Fjellanger
June 2022

Norwegian University of Science and Technology
Faculty of Information Technology and Electrical Engineering
Department of Electric Power Engineering

Voltage distribution in medium voltage machines for aerospace applications fed by power converters

Per Henning Hammerstad Møllevold

Department of Electric Power Engineering

Norwegian University of Science and Technology

Trondheim, Norway

Supervisors: Pål Keim Olsen, Njål Rotevatn and Viljar Fjellanger

Company: Rolls-Royce Electrical Norway AS

Abstract—The thesis describes a detailed *MATLAB & Simulink* based model for predictions of the voltage distribution of windings exposed to repeatedly steep fronted surge voltages generated by a PWM inverter. The proposed model is a *Lumped parameter equivalent* consisting of RLC parameters. The frequency dependency of the parameters was calculated both analytically and with the help of the *Finite element method* in the simulation software *COMSOL Multiphysics*[®]. Finally, the model was validated through two experiments conducted on three different winding configurations. The first validation measured the frequency impedance response of the winding, and a second validation compared the simulated and measured voltage distribution of inverter fed windings. The model showed the best performance for both validations utilising stationary parameter values for air coils. Although the simulated results gave a reasonable degree of confidence in the proposed model, further testing and investigations are required for the model to be valid in more complex contexts.

Index Terms—Lumped parameter equivalent model, machine winding, steep fronted surge voltage, voltage distribution, turn-to-turn voltage, PWM inverter fed winding, impedance response.

I. INTRODUCTION

An important factor for the development of *all-electric aircraft* (AEA) is the design of electrical machines. Today's trends suggest medium voltage DC power systems are advantageous compared to medium AC power systems in AEA's [1]. The standard is 540V DC ($\pm 270V$), however, voltage levels in the *kV* range are now being suggested [2], [3]. The emerging *wide-bandgap* (WBG) semiconductors such as *Silicon Carbide* (SiC) and *Gallium Nitride* (GaN) introduces the possibility to increase the efficiency and the power density [1]. These semiconductors have low switching losses and enable higher switching frequencies, creating high dV/dts in operation.

With this in mind, extra attention to the design of the machines, windings and insulation system is necessary. The higher the altitude, the lower the breakdown voltage. The minimum voltage for the occurrence of the electrical arcing phenomena can be calculated according to Paschen's law [2]. Therefore, it is crucial to have accurate predictions of the voltage distribution in the machine's windings. In this way, voltages higher than the *Partial Discharge Inception Voltage*

(PDIV) where degrading of the insulation occurs can be avoided [1].

The common models for investigation of voltage distribution of windings exposed to steep fronted voltage surges are the *Multiconductor transmission line theory* (MTLT) [4], [5] and the *Lumped parameter equivalent circuit model* [6]–[8]. Recently, powerful calculations tools have been increasingly applied, such as *Ansys* and *COMSOL*, which utilise the *finite element method* (FEM). The advantage these programs offer, is that it is possible to effectively represent and study exact models of complicated real winding configurations [9].

Numerous papers have investigated the effects of surge voltages in stator windings to prevent machine failure. The unevenly distributed voltage in the machine's windings is highest in the first coil between the last turns [5], [10]. The work done in [11] shows the importance of developing good models. They tested several models found in the literature, which gave different results, especially for the turn-to-turn and the turn-to-ground voltages. This thesis aims to investigate and predict the voltage distribution in medium voltage machines for aerospace applications based on a developed *Lumped parameter equivalent model*.

The thesis starts by presenting today's trends for all-electric aircraft architecture. Then, the theory of the transient phenomena and the voltage distribution caused by repetitive switching pulses applied to the machine's windings is described. Further, the methods for three experimental parts of the thesis are presented. The first part is a parameter study, estimating the parameters in the proposed *Lumped parameter equivalent model*. The following two parts are the laboratory experiments used to validate the proposed model. Three different winding configurations are investigated. The first validation measures the frequency impedance response of the winding and the second validation compares the simulated and measured voltage distribution of inverter fed windings. Next are the results presented and discussed, followed by a more general discussion regarding the model choices and the experiments. Finally, the conclusion of the work is presented, along with a proposal for further work.

mds

June 5, 2022

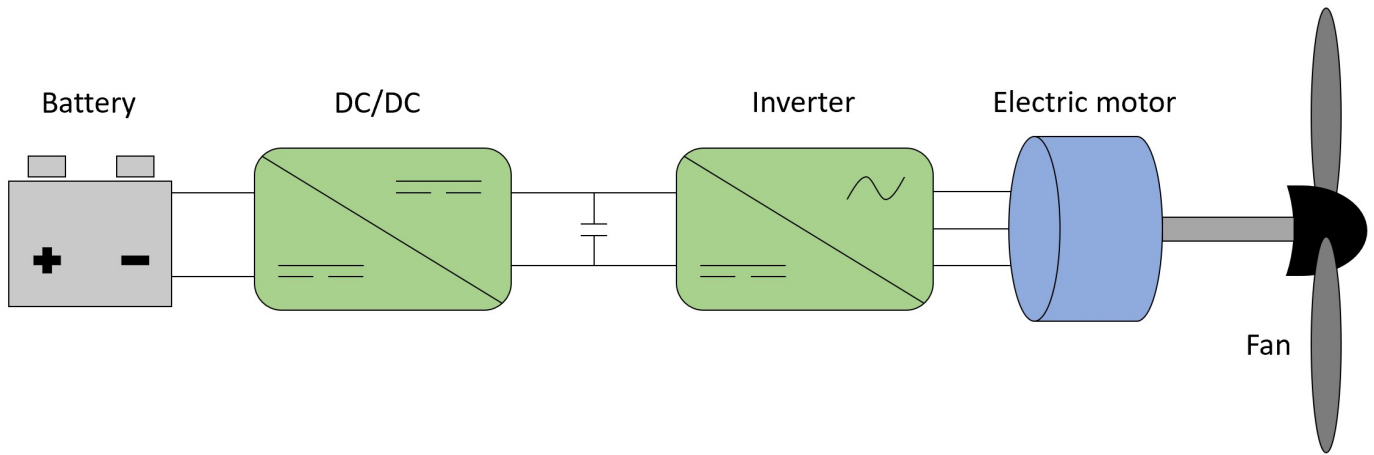


Fig. 1. All-electric aircraft powertrain architecture [1].

II. THEORY

This section includes a description of the architecture of an all-electric aircraft. Furthermore, presenting the theory of voltage surges before addressing the voltage distribution and possible stresses in the machine winding. Finally, this section presents the theory of the lumped parameter equivalent circuit model.

A. Architecture of an all-electrical aircraft

The only energy source used onboard an all-electric aircraft is a set of battery energy storage devices. Consequently, the AEA can achieve zero emissions. The following subsections will give a brief description of the different components in the block diagram of the AEA powertrain architecture shown in Fig. 1.

1) *Battery*: The energy and power density of the storage systems are the most important parameters of the aircraft. It determines the number of passengers the aircraft can carry and the range the aircraft can travel. With today's technology, an AEA will be able to carry 20-30 passengers a distance of approximately $>483km$, or ten passengers $>966km$ [12]. Therefore, as indicated by Fig. 2, the development of AEAs are fully dependent on advancing high-power density battery technologies. The lithium-ion (Li-ion) battery is the state-of-the-art battery technology for automotive applications. Additionally, Li-ion batteries have the highest energy density ($110-160Wh/kg$), power density ($1800W/kg$) and efficiency (80%) compared to other battery types [1].

2) *DC/DC Power converters*: The DC/DC converter creates a DC-bus system for the supply of voltage in the aircraft. Utilising a buck-boost DC/DC converter can manage the voltage at the desired level [13]. The DC-bus voltage is suggested to be in the medium voltage range. Medium voltage DC (MVDC) systems have the following advantages compared to the existing DC ($\pm 270V$) and low voltage AC systems [1]:

- *Reduced cable weight and cost*: The transmission line system contains only a positive conductor and a ground.

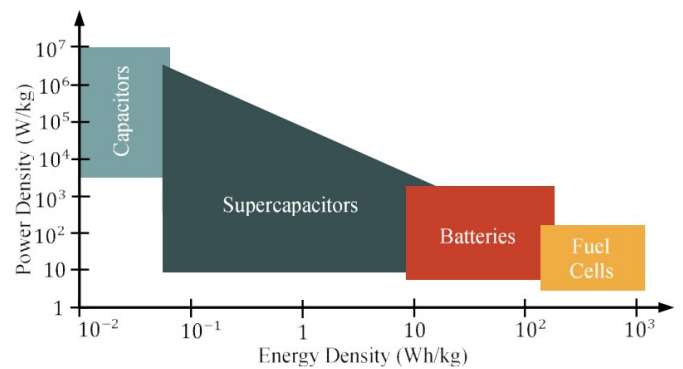


Fig. 2. Comparison of the power and energy density of several energy storage options [1].

In comparison, an AC system needs three-phase conductors in its transmission line system.

- *Eliminates the skin effect and proximity effect losses*: In AC systems, high frequencies are used to reduce the size of magnetic components such as electrical machines or transformers. Consequently, significant skin effect and proximity effect losses occur in the conductors.
- *Lower corona effect*: The resulting dV/dts created by modern semiconductor devices with higher voltage and faster switching pose more challenges to the insulation design if using a *medium voltage AC* (MVAC) system.

Nevertheless, the disadvantages pose challenges to the development of MVDC systems [1]:

- *Increased insulation stress*: The breakdown voltage is lower for higher altitudes. The Paschen curve can determine the partial discharging inception voltage.
- *Fault protection in MVDC systems*: There does not exist a natural zero crossing in the current required for contact separation in the circuit breakers. Therefore, various solutions have been developed, e.g. hybrid circuit breakers and solid-state circuit breakers.
- *Cosmic ray impact on high voltage semiconductor de-*

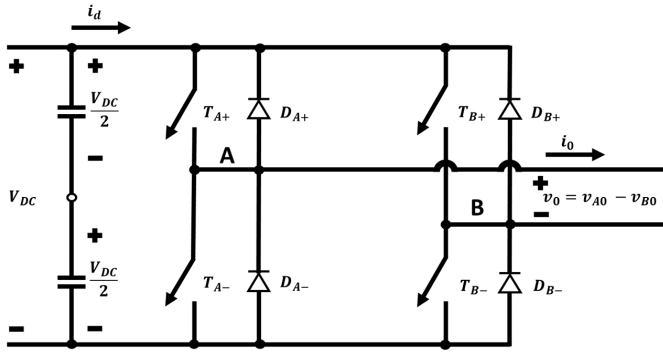


Fig. 3. Single-phase full-bridge inverter [13].

ices at high altitudes: It has been reported in [14] that intensive cosmic rays at high altitudes may damage semiconductor devices.

3) *Inverter*: Conversion to pure sine waves is necessary for the operation of a *Permanent magnet synchronous machine* (PMSM), which is one of the most attractive candidates for the aircraft industry [2]. Aiming at high reliability and low weight for high power applications has *silicone carbide metaloxide semiconductor field effect transistors* (SiC MOSFET) using *pulse-width modulation* (PWM) proven to be beneficial compared to other power electronic technologies [15]. Additionally, the inverter topology needs to enable unipolar operation to allow for regenerative braking [3]. Bipolar switching is an alternative. However, unipolar switching devices are favourable since it has lower switching losses and low conduction losses even at high temperatures [15]. The capability of a SiC MOSFET rated at a voltage level of 1200V has been demonstrated to generate pulses with $<5\mu s$ durations. However, SiC MOSFETs can operate at frequencies up to 2kHz, at temperatures up to 200°C and voltages up to 10kV in normal operations in high power applications [15].

4) *Electric motor*: Several reviews and evaluations of performances to conclude which electrical machine is best suited for aerospace applications have been conducted [1], [2], [16]. The studies concluded that PM machines are the clear frontline in achieving multiple desirabilities for the aviation industry. This machine offers high power density and efficiency compared to other machines. However, at the expense of higher costs because of the PM materials utilised in their construction [1].

B. Voltage surges

This section explains the generation of voltage surges. Surge propagation from the inverter to the motor coils will also be addressed.

A PWM inverter generates repeatedly short pulses of high voltage, which propagates from the drive through a cable to the motor. In Fig. 4 is the pure sine wave PWM conversion for unipolar voltage switching illustrated for a single-phase full-bridge inverter as shown in Fig. 3. Switches T_{A+} and T_{A-}

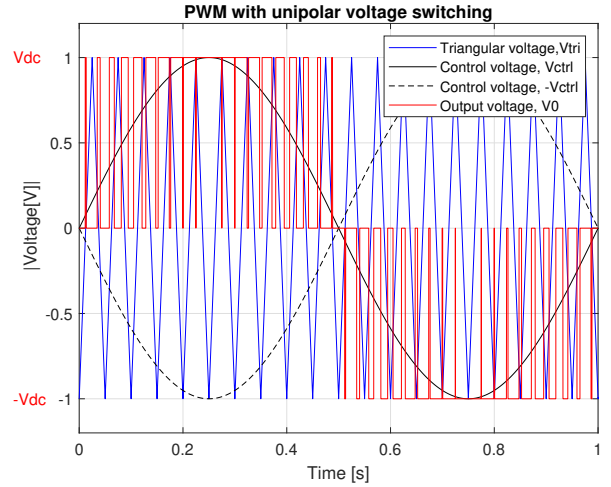


Fig. 4. Simulated PWM signal for a single-phase full-bridge unipolar voltage switching inverter.

are forming switching leg A, and T_{B+} and T_{B-} are forming switching leg B. Whenever the sinusoidal signal (black) is higher than the triangular waveform (blue) is T_{A+} in the high state (1), and the T_{A-} is in the low state (0). When the sinusoidal signal (dashed black) is higher than the triangular waveform is T_{B+} in the high state (1), and the T_{B-} is in the low state (0). The resulting PWM signal plotted in red is the output voltage $v_0 = v_{A0} - v_{B0}$ [13].

The inverter output pulse travels from the drive to the motor through a cable of length l with a propagation time t_p defined as in (1). The wave propagation velocity is a function of the cable inductance per unit length, L_0 , and the cable capacitance per unit length, C_0 . The velocity can also be defined in terms of permeability, $\mu = \mu_0\mu_r$, and permittivity, $\epsilon = \epsilon_0\epsilon_r$, of the dielectric materials between conductors. Setting $\mu_r = 1$ results in a function dependent on the speed of light ($c = 3.0 \cdot 10^8 m/s$) and the relative permittivity ϵ_r for the velocity, v , as shown in the last step of (2) [17].

$$t_p = \frac{l}{v} \quad (1)$$

$$v = \frac{1}{\sqrt{L_0 \cdot C_0}} = \frac{1}{\sqrt{\mu \cdot \epsilon}} = \frac{c}{\sqrt{\epsilon_r}} \quad (2)$$

The travelling wave must traverse the cable four times to complete one oscillation cycle. Therefore, the cycle time is related to the propagation time and the cable length, $T_{cycle} = 4 \cdot t_p$. The oscillation frequency, f_0 , is inversely proportional to the cable length. Consequently, higher oscillation frequencies occur for shorter cable lengths, as implied by (3). Because of the cable oscillation frequency, the characteristics of the over-voltage transient are damped by skin and proximity effects. However, if the natural frequency of the cable corresponds to the natural frequency of the winding, high internal overvoltages may develop [18].

$$f_0 = \frac{1}{T_{cycle}} = \frac{1}{4 \cdot t_p} = \frac{v}{4 \cdot l} = \frac{1}{4 \cdot l \cdot \sqrt{L_0 \cdot C_0}} \quad (3)$$

There is a direct relationship between the overvoltage occurring at the winding terminals of the electrical machine and the length of the cable connecting the inverter and the motor [19]. The reflected waves travelling over the connecting cable amplify the voltage supplying the electrical machine. When a voltage waveform travels from the inverter to the motor along a transmission line that does not terminate at its characteristic impedance, the wave is reflected when it encounters the first discontinuity. The reflection coefficient, ρ , is defined as the ratio between the reflected wave and the incoming wave given in (4).

$$\rho = \frac{u_{ref}}{u_{inc}} = \frac{Z - Z_{cable}}{Z + Z_{cable}} \quad (4)$$

Assuming that the motor impedance is much greater than that introduced by the cable ($Z \rightarrow \infty$) gives a reflection coefficient, ρ_m , equal to 1. Additionally, assuming that the impedance of the inverter is much smaller than the impedance of the cable ($Z \rightarrow 0$) gives a reflection coefficient, ρ_i , equal to -1 [19]. This impedance mismatch between motor, cable and inverter can cause overvoltages up to 2 per unit of the bus voltage [17].

The length of the cable should be less than the critical length derived in (5) [19].

$$t_r = 2 \cdot t_p = \frac{2 \cdot l_{critical}}{v} \rightarrow l_{critical} = \frac{v \cdot t_r}{2} \quad (5)$$

where t_r is the voltage rise time and $l_{critical}$ is the critical length of the cable. For cables shorter than the critical length, no overvoltages above 2 per unit will occur at the motor terminal [17].

In this thesis, preventative measures are taken to ensure that the cable length is shorter than the critical cable length given by (5). In this manner, overvoltages above 2 per unit caused by the reflected waves propagating in the cable are prevented. Minimizing the cables' length between the inverter and the motor will also be the recommended practice in the realization of AEAs.

C. Voltage distribution and stresses

Apart from the overvoltages caused by the cable, there are other phenomena causing stress to the machine winding and insulation systems. Non-uniform distribution of voltage might lead to partial discharges, which is considered another leading cause of the increased electrical stress on the insulation system. The non-uniform voltage distribution in the turns of a coil is the consequence of the parasitic capacitance introduced by the insulation, which has a significant value at high frequencies.

$$\omega L \gg \frac{1}{\omega C} \quad (6)$$

At high frequencies, the inductive elements have less importance for the voltage distribution seen by (6). Therefore, the capacitive elements dominate the response of the voltage impulse with short rise times. The voltage distribution depends on the turn-to-turn and turn-to-ground capacitance, the capacitance between windings, and the capacitance between

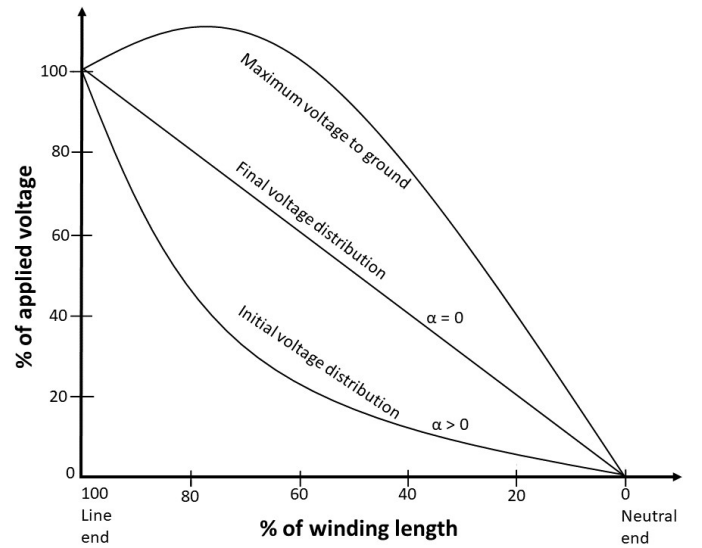


Fig. 5. Impulse voltage distribution of a winding; extrapolated from [18].

windings and ground. This is because the current cannot be established instantaneously in inductance, and the magnetic field requires a finite time to build up [18]. The ratio $\sqrt{C_G/C_S}$ characterize the initial voltage distribution. It is known as the distribution constant, α , and is derived from a time-domain analysis of a winding [18]. C_G and C_S are the machine winding's total ground capacitance and series capacitance. For a given length of the winding, L , is the uniform gradient for the unit amplitude surge α/L . Thus, the maximum initial gradient is at the end α [18].

The distribution constant indicates the degree of deviation of the initial voltage distribution from the final linear voltage distribution, which is solely decided by the inductance of the winding. During the transient period, the voltage readjusts itself from the initial to the final value, as shown in Fig. 5. Here is a continual interchange of energy between electric and magnetic fields. The transient is oscillatory because of the low damping factor of the windings. Hence, the voltage at any point oscillates about the final voltage value. The higher the value of α , the higher the deviation and amplitudes of oscillations. Therefore, any change in machine design, which decreases the distribution constant of the winding, results in a more uniform voltage distribution and reduces the voltage stresses between different parts of the winding [18].

Additionally, the first and last coils of the winding are often placed next to each other by construction and separated by a thin layer of insulation. In this situation, the highest voltage occurs, which can cause insulation breakdown [19].

IEC Standard 60034-18-41 have listed the significance of different factors that can affect the lifetime of the insulation system [20]. For the main wall insulation and the phase-to-phase insulation, the peak impulse voltage for both fundamental and impulse frequency is most significant. The jump voltage and the rise time is most significant for the turn-to-turn insulation. Other factors deemed less significant for

the insulation system are the fundamental frequency and the impulse voltage repetition rate.

D. Lumped parameter equivalent circuit

This section presents the theory of the *Lumped parameter equivalent circuits*. Additionally, the travelling waves inside the winding and what they imply for the modelling are described.

Equivalent circuits provide great convenience and reliability to simulation, analysis and calculation. There are two kinds of equivalent circuits, the lumped parameter circuit and the distributed parameter circuit. The lumped parameter circuits are simple and popular in practical analysis and calculations. However, when researching travelling waves, are distributed parameters preferred. In comparison to the lumped parameter circuits, the corresponding equations for distributed parameters are very complex for analysis [21].

Of the different lumped parameter equivalent circuit representations presented in Fig. 6 is Fig. 6(b), the π model, the best equivalent [21]. In the coils analysis, each turn is considered a transmission line. The resulting lumped circuit for a model of a winding contains turn inductance, resistance, mutual inductance, and turn-to-ground and turn-to-turn capacitance. This approach is valid when each element of the equivalent circuit represents a portion of the coil much smaller than the wavelength at a frequency corresponding to the fast overvoltages considered [6].

The speed of the wave travelling inside the winding can be determined by (2). The wavelength, λ , can be calculated from the speed using (7).

$$\lambda = \frac{v_{winding}}{f_{max}} \quad (7)$$

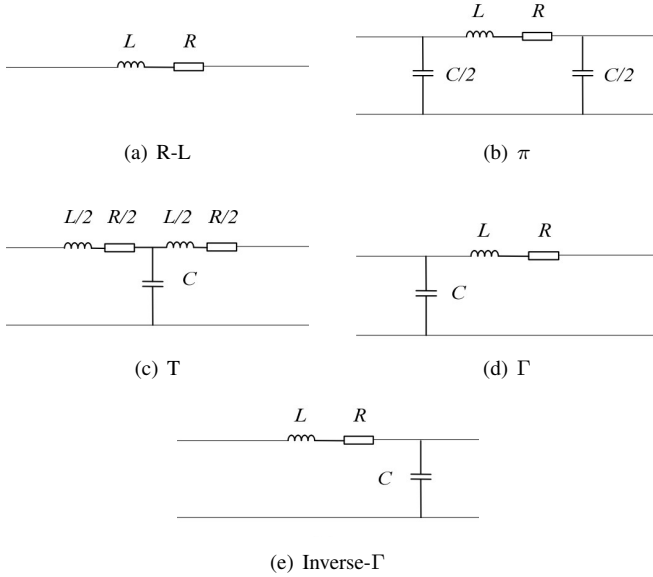


Fig. 6. Lumped parameter circuits of transmission lines; extrapolated from [21]

where f_{max} is the maximum frequency of the input signal. For switching pulses from a source inverter, the frequency can be approximated by the inverse of the maximum rise time, t_r , of the voltage pulse [22]. The maximum frequency can be approximated using (8).

$$f_{max} \approx \frac{1}{t_r} \quad (8)$$

The voltage distribution inside a part of the winding can be assumed to be constant and equally distributed for a length of less than 1/10 of the signal wavelength [23]. For maximum rise times of $10ns-50ns$ with relative permittivity $\epsilon_r = 6$ implies that the voltage distribution is evenly distributed for a maximum length of the winding conductor of approximately $0.122m-0.612m$. However, if the length of one turn is more than 1/10 of the wavelength, even further sectioning is needed.

III. METHOD

This section presents an analytical approximation method for finding the parameters in the proposed equivalent circuit model. Furthermore, the different winding configurations used in this study are included, followed by a description of the utilisation of *COMSOL* to approximate the parameters in the proposed equivalent model. Then, the proposed *Lumped parameter equivalent circuit* model is presented along with the assumptions and simplifications for the model. Moreover, the two experimental setups will be described in detail, first for the impedance frequency response and finally for the PWM inverter fed winding.

A. Analytical calculation of the electrical parameters of the winding

In order to obtain a detailed model, is the series impedance and the admittance matrices $[\mathbf{Z}]$ and $[\mathbf{Y}]$ required. The general formulation in (9) calculates them.

$$\begin{aligned} [\mathbf{Z}] &= [\mathbf{R}] + j\omega[\mathbf{L}] \\ [\mathbf{Y}] &= [\mathbf{G}] + j\omega[\mathbf{C}] \end{aligned} \quad (9)$$

where $[\mathbf{R}]$, $[\mathbf{L}]$, $[\mathbf{G}]$ and $[\mathbf{C}]$ are the series resistance, series inductance, parallel conductance and capacitance matrices, respectively. This section describes how these matrices can be calculated and how they can be utilised to create a lumped parameter equivalent circuit.

1) *Capacitance*: The turn-to-turn and the turn-to-ground capacitance can be calculated directly with the help of the parallel plate approximation [24]. (10) includes the insulation thickness h and the insulation permittivity ϵ , in addition to the length of the conductor surface a and the length of the section of the turn d for the capacitance that is wanted to calculate. The permittivity, ϵ , is the product of the relative permittivity of the insulation material, ϵ_r , and the vacuum permittivity, ϵ_0 .

$$C = \epsilon \cdot \frac{a \cdot d}{h} \rightarrow C' = \epsilon \cdot \frac{a}{h} \quad (10)$$

where C' represents the capacitance per unit length.

The calculations can form the Maxwell capacitance matrix $[\mathbf{C}_0]$. The diagonal elements $C_{0,xx}$ consists of the capacitance between conductor x and ground and a summation of the capacitances between turn x and other turns. The off-diagonal elements $C_{0,xy}$ are the negative of the mutual capacitance between turn x and y , respectively.

2) *Conductance*: Once the capacitance matrix has been calculated, the conductance matrix can be obtained using (11).

$$[\mathbf{G}] = \omega[\mathbf{C}] \tan(\delta) \quad (11)$$

where $\tan(\delta)$ is the loss tangent for the dielectric material used as the electric insulator and ω is the angular frequency. The loss tangent is calculated using (12) [25].

$$\tan(\delta) = \frac{\sigma}{\omega\epsilon} \quad (12)$$

where σ is the conductivity, and ϵ is the permittivity of the dielectric material.

3) *Inductance*: There are three contributors to the coil self-inductance [26]. L_{iron} is the contribution to the self-inductance due to the flux penetration into the iron core per unit length, calculated by (13).

$$L_{iron} = \frac{\mu \cdot n^2 \cdot p}{z} \quad (13)$$

where $p = \sqrt{\rho/(\pi f \mu)}$ is the depth of penetration, n is the number of turns in the coil, z is the slot perimeter, μ is the iron permeability, ρ is the iron resistivity and f is the frequency [26].

The inductance caused by flux in the insulation material between turns and the slot walls and wedges, L_{ins} , can be approximated quite accurately with (14) or (15) in combination with (16) [18], [27]. In [27] are simple inductance formulas for different kinds of winding configurations presented. (14) gives accurate approximations of the total inductance for coils where the three terms in the denominator are about equal.

$$L_{ins} = \frac{1}{0.0254} \frac{0.8 \cdot a^2 n^2}{6a + 9b + 10c} [\mu H] \quad (14)$$

where a is the geometric mean radius of the winding, b is the total width of the coil, c is the total height of the coil, and n is the number of turns.

Kulkarni's method calculates self-inductance and mutual inductance for windings with square-shaped conductors. The self-inductance of a single turn of a circular coil with square cross-section with square side length c and average radius a is given by (15) [18].

$$L_{AA} = \mu_0 \cdot a \left[\frac{1}{2} \left(1 + \frac{1}{6} \left(\frac{c}{2a} \right)^2 \right) \ln \left(\frac{8}{(c/2a)^2} \right) - 0.84834 + 0.2041 \left(\frac{c}{2a} \right)^2 \right] \quad (15)$$

This equation applies for relatively small cross-sections such that $(c/2a) < 0.2$. If the cross-section is not square, it should be divided into several square cross-sections.

The mutual inductance between two conductors with radii R_A and R_B with a distance S between them is given in SI units as (16) [18].

$$L_{AB} = 4\pi\sqrt{R_A R_B} \left[\left(\frac{2}{k} - k \right) \cdot K(k) - \frac{2}{k} \cdot E(k) \right] [nH] \quad (16)$$

where

$$k = \sqrt{\frac{4R_A R_B}{(R_A + R_B)^2 + S^2}} \quad (17)$$

and $K(k)$ and $E(k)$ are the complete elliptic integrals of the first and second kinds.

(15) and (16) applies for thin circular filaments of negligible cross-section. For circular windings of rectangular cross-sections, Lyle's method can be used in combination with (15) and (16) to give more accurate approximations. The two turn's cross-sections are represented as two equivalent filaments. The adjustments change the radius, R , and the distance between them, S , as shown in (18).

$$R_{new} = R_{old} \left(1 + \frac{h^2}{24 \cdot R_{old}^2} \right) \quad (18)$$

$$S = 2\sqrt{\frac{w^2 - h^2}{12}}$$

where w is the total width occupied by the two turns where any gaps with insulation between them are included and h is the length of the shortest edge of the rectangular cross-section. It should be noted that this adjustment is most frequently used for the type of winding configuration investigated in this thesis, where $w > h$. If $w < h$ should h be used instead of w and w be used instead of h in (18) [28].

The skin effect is the last contribution to the inductance. It can be approximated by using (19).

$$Z_{sk} = \frac{h}{a \cdot \xi \cdot \sigma} \quad (19)$$

where σ is the copper conductivity, a is the perimeter of the turn, h is the height of the turn and the complex skin depth ξ for copper conductors is as in (20) [29].

$$\xi = \sqrt{\frac{2 \cdot (1 + j)}{\omega \cdot \mu \cdot \sigma}} \quad (20)$$

where ω is the frequency and μ is the permeability of copper.

The inductance per unit length is the sum of the three contributions presented in (13), (19) and (14). The third term containing (14) can be substituted with Kulkarni's approach in (15) and (16).

$$L_t = L_{iron} + \frac{L_{ins}}{n \cdot l} + \Im(Z_{sk}) \quad (21)$$

Another approach for estimation of the inductance, which is often used for *MTLT* is shown in (22) [29].

$$[\mathbf{L}] = \frac{\epsilon_r}{c^2} [\mathbf{C}_0]^{-1} \quad (22)$$

where c is the speed of light and $[\mathbf{C}_0]$ is the Maxwell capacitance matrix. This method will not be used in this study.

4) *Resistance*: The conductors in the winding offer higher resistance for an alternating current than for a direct current. The increase in resistance is caused by the skin and proximity effects and hysteresis and eddy current losses in nearby ferromagnetic materials. The skin effect describes the phenomena of current flowing closer to the conductor's surface for a higher frequency of alternating currents. The proximity effect is caused by induced currents flowing in adjacent conductors, resulting in a distortion of the cross-sectional current distribution in the conductors. According to Lenz's law, Eddy currents are induced in conductive ferromagnetic material when exposed to AC magnetic fields. These currents circulate within the material, dissipating power because of the resistivity of the material [30].

Dowell's formula has been found to reliably predict the increased resistance in cylindrical windings where the layer thickness is less than 10% of the radius [31]. The resistance for sinusoidal excitation, accounting for both skin and proximity effects, can be approximated with (23).

$$R_{ac} = R_{dc} \cdot \left(1 + \frac{\Psi}{3} \Delta^4\right) \quad (23)$$

where

$$\Psi = \frac{5p^2 - 1}{15} \quad (24)$$

where p is the number of layers in the winding and Δ is the ratio of the layer thickness d to the skin depth δ .

$$\delta = \sqrt{\frac{2}{\omega\mu_0\sigma}} = \frac{1}{\sqrt{\pi\mu_0\sigma f}} = \sqrt{\frac{\rho}{\pi\mu_0 f}} \quad (25)$$

where σ is the conductivity of copper, ρ is the resistivity of copper, f is the frequency and $\omega = 2\pi f$.

$$\Delta = \frac{d}{\delta} \quad (26)$$

The DC resistance is

$$R_{dc} = \frac{\rho l}{A} = \frac{\rho l}{wh} \quad (27)$$

where A is the cross-section area of the conductor with height h and width w . l is the length of the winding.

However, if the winding is placed inside a slot, the eddy currents and hysteresis losses must be accounted for. The method for calculating the slot resistance, R_{st} , is presented by Hanselman, and it is dependent on the effective eddy current resistance, R_{ec} , and the slot resistance, R_s [30]. This was the method used to approximate the resistance in the author's previous work.

$$R_s = \frac{\rho n^2 l}{k_{cp} w_s h_s} \quad (28)$$

$$R_{ec} = \frac{h_s l h^2 n^2}{9\sigma \delta^4 w_s} \quad (29)$$

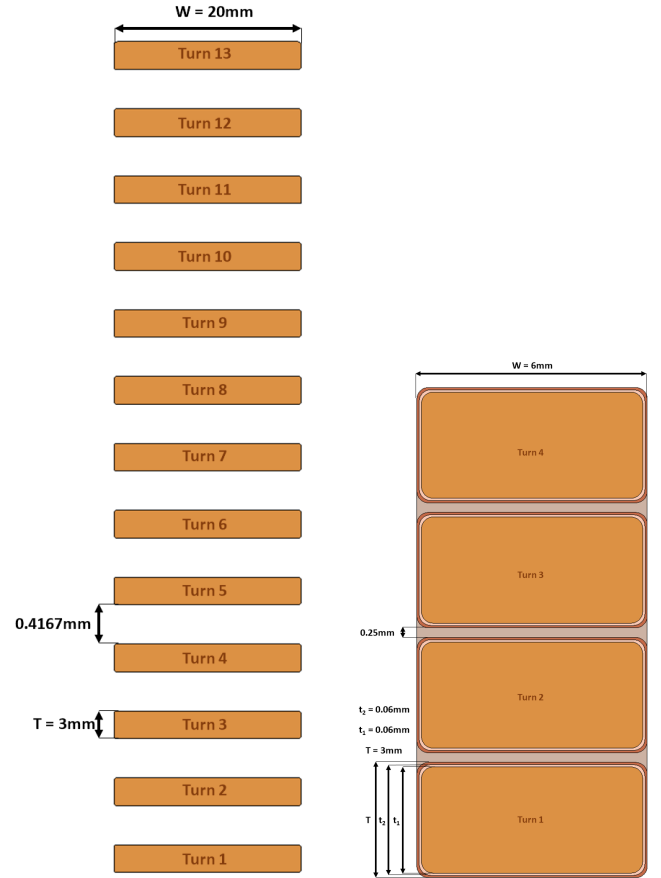
$$R_{st} = R_s + R_{ec} = R_s \left(1 + \Delta_e\right) = R_s \left(1 + \frac{1}{9} \left(\frac{h_s}{\delta}\right)^2 \left(\frac{h}{\delta}\right)^2\right) \quad (30)$$

where w_s and h_s are the width and height of the slot the winding is placed in, and k_{cp} is the fill factor of copper in the slot.

B. Winding configurations

This section describes the three different winding configurations used in the experiments in terms of dimensions and material properties. Additionally, a description of C-ferrite cores used to increase the inductance of the two and four turn winding is included.

1) *Two and four turn winding configuration*: Two windings using the same wires have been constructed. The copper wire is *Isodraht* and has a width of 6mm and a height of 3mm [32]. Both windings are wound as cylindrical windings with a radius of 50mm (geometric mean radii, $\text{GMD} = 53\text{mm}$). Every turn is placed on top of each other and separated by a thin layer of *LOCTITE 435 HURTI GLIM*. The layer has been measured to be approximately 0.25mm . The dielectric constant of the layer is $\epsilon_r = 2.75$ [33]. In addition, there is a basecoating; polyester amide (*PEA*) with dielectric constant assumed to be $\epsilon_r = 3.5$ and an overcoating; polyamide-imide (*PAI*) with dielectric constant assumed to be $\epsilon_r = 2.5$ [34]. Each coat is approximately equal $t_1 = t_2 = 0.06\text{mm}$. Fig. 7(b) shows a cross-section representation of the four turn winding configuration. The two turn winding configuration would have



(a) A 2D representation of the 13 turn winding configuration in COM-SOL. (b) A 2D representation of the four turn winding configuration in COM-SOL.

Fig. 7. Two different winding configurations in a 2D illustration.

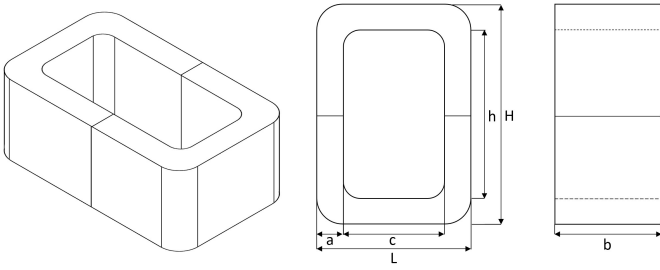


Fig. 8. Illustration of the C-ferrite cores and their dimensions.

TABLE I
DIMENSION OF THE LAMINATED C-IRON CORES.

Dimension [cm]					
H	h	L	a	b	c
12.6	8.8	7.4	1.9	3.8	3.6

been the same as Fig. 7(b) without turn three and four, and their insulation. Fig. 21 and Fig. 22 in Appendix A shows real picture representations of the two different configurations.

C-ferrite cores have been used to increase the inductance of the winding. In total, eight C-ferrite cores are used to construct four pairs. The dimension of one pair is shown in Tab. I. Fig. 8 gives an illustration of the shape of the core and notations used in Tab. I. Fig. 23 in Appendix A shows the four turn winding with half the C-cores included.

2) *Thirteen turn winding configuration*: The third test object is a set of three equal windings constructed by ABB Group, former ASEA. The wires have a width of 20mm and a height of 3mm . The wires do not have any coating and are wound as cylindrical windings with a radius of 33.5mm ($\text{GMD} = 43.5\text{mm}$) with 4.167mm of air separating each turn. Fig. 7(a) and Fig. 9 shows a 2D and a 3D model of the winding. Fig. 24 in Appendix A shows a real picture representation of the thirteen turn winding configurations.

This winding configuration is not fully thirteen turns, meaning that the wires do not fully complete the thirteenth turn. When modelling and estimating the parameters of the winding, the winding is considered to have thirteen turns. However, the first and last turn of the winding will have reduced its parameters in the *Lumped equivalent parameter model* such that they are closer to the actual winding.

C. The utilisation of COMSOL for calculating parameters

This section describes how *COMSOL* is utilised to obtain the *RLC* parameters of the desired coil configuration. Different physics are being used to obtain the parameters. Therefore, the first section describes how capacitance is obtained. Followed by how the inductance and resistance are obtained.

1) *Capacitance*: There is a special study step for efficient calculation of capacitance matrices in the physics *Electrostatics & Electrostatics, Boundary Elements, Stationary Source Sweep* is the study that identifies all terminals, domains or boundaries in the model and excites them one at a time using

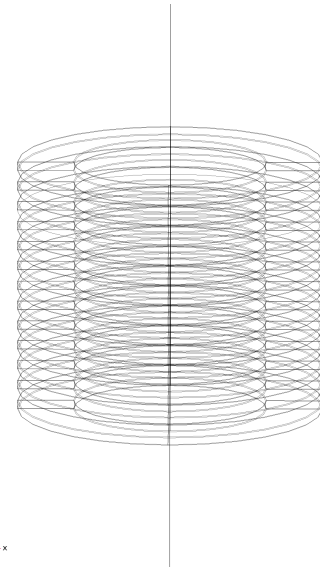


Fig. 9. A 3D representation of the thirteen turn winding in *COMSOL* (physics: *mfco*).

a fixed charge or current. While one *Terminal* is excited, the others will be floating with zero net charge/current [35].

In principle, the capacitance is calculated based on the relationship in (31).

$$\vec{Q} = [\mathbf{C}]\vec{V} \quad (31)$$

When the study is completed, the *Inverse Maxwell capacitance matrix* can be obtained from a *Global Matrix Evaluation* of the derived values of the results. It has a built-in post-processing function that can transform the *Inverse Maxwell capacitance matrix* into the *Maxwell capacitance matrix* or the *Mutual capacitance matrix*. It is important to note that in order to get a proper matrix definition, at least one *Ground* node should be specified in the model [35].

Fig. 7(b) and 7(a) shows the 2D models used for two of the test objects for the capacitance calculations. The windings are represented using the exact geometric dimensions of the conductors and measurements of the coil. The *Ground* node is usually located at the slot surfaces in real machines. However, in this study, the ground node is placed somewhere at the same distance as the grounded location in laboratory experiments ($\approx 30\text{cm}$ away from the test object). This ensures a low distribution constant. Hence, the initial voltage distribution is expected to be close to the final voltage distribution, as illustrated in Fig. 5.

2) *Inductance*: There are several possible options for how *COMSOL* can be utilised to obtain the inductance. The physics *Magnetic Fields, Current Only (mfco)* interface solves Ampère's law in the main node *Free Space* feature using the magnetic vector potential as the dependent variable. *mfco* is designed to compute the lumped inductance matrix of complex winding configurations efficiently [35]. The self-inductance and mutual inductance in matrix form are calculated using a *Stationary Source Sweep* study. From a *Global Matrix*

Evaluation of the derived values of the results are the matrix obtained. When modelling the cylindrical winding configurations in *mfco*, the 2D cross-section model as shown in Fig. 7 is revolved 359° . Moreover, a sphere is added to the geometry. Fig. 9 shows the 3D model for the thirteen turn winding, where the sphere surrounding the winding has been hidden. The inductance matrix from the results can be scaled to represent 360° .

From the inductance matrix can the mutual coupling factor, k , be extracted using (32).

$$L_{AB} = k_{AB} \cdot \sqrt{L_{AA} \cdot L_{BB}} \quad (32)$$

where k_{AB} represents the mutual coupling factor for the turns of interest.

The total inductance of the winding can be calculated with (33) [28]. It calculates the coil inductance from the inductance matrix.

$$L_{eq} = n \cdot L + 2 \cdot \sum_{i=1}^{n-1} (n-i) \cdot M_i \quad (33)$$

where M_i is the mutual inductance between pairs, L is the self-inductance of a single turn and n is the number of turns.

It should be noted that this only gives accurate results for winding configurations where turns have equal self-inductances. Therefore, when simulating in *COMSOL Magnetic Fields (mf)*, this assumption helps to quickly obtain the inductance matrix to be used in the lumped parameter model.

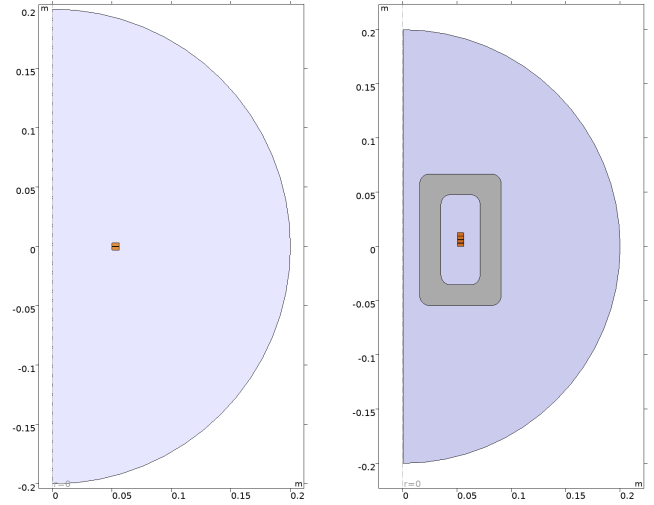
The physic *Magnetic Fields (mf)* is used both to catch the stationary and the frequency dependency of the parameters. The winding is modelled in a *2D Axisymmetric* model. Because of the circular shape of the winding, this model can compute the solution significantly faster than if a *3D* model was used.

This physics interface solves Maxwell's equations. Similar to *mfco*, *mf* uses the magnetic vector potential as the dependent variables. However, the scalar electric potential can be used as the dependent variable for coils [35]. In Fig. 10(a) is the two turn winding represented without the iron, and in Fig. 10(b) is the four turn winding presented with the iron. The thirteen turn winding is not shown because it would look the same as Fig. 10(a), but with additional turns with different dimensions.

When simulating a *Stationary* study with each turn represented as a coil, the *Concatenated flux* can be obtained for each turn. In the case of single conductor coils, it is the self-inductance of the concatenated flux divided by the applied current.

Alternatively, a *surface integration* of the *Magnetic energy density* can obtain the total inductance of the coil. It is also possible to extract the total magnetic energy density directly from a *Global Evaluation (mf.intWm)*. The integration is multiplied by two and divided by the square of the current, equal 1A if not changed ($W = 1/2 \cdot LI^2$).

Another approach to obtaining the coil inductance in *mf* is to extract it directly from the results. The coil inductance can be found among the *Derived values* in a *Global Evaluation*.



(a) The two turn winding configuration without iron. (b) The four turn winding configuration with iron.

Fig. 10. The two winding configurations modelled in a 2D Axisymmetric in *COMSOL*.

3) *Resistance*: The resistance can be obtained from *Magnetic Field (mf)*, *Magnetic Fields, Currents Only (mfco)* and the *Electric Currents (ec)* physics. When following the above descriptions of the modelling in the different physics, the resistances can be found as either a *Global Evaluations* or a *Global Matrix Evaluation*.

4) *C-cores included in the 2D Axisymmetric model*: To account for the iron is an additional *Component* defined. Therefore, the model consists of two *Components*, one where the winding is only surrounded by air, and one where the C-core encloses the coil, as shown for the two and four turn winding models in Fig. 10(a) and Fig 10(b), respectively. The results from the two different *Components* are added together by scaling their values after how big a portion their sectors cover. For four pairs of C-cores enclosing the two and four turn winding configuration, the sector angle is derived as follows:

$$\text{part} = (2 \cdot 4) \arctan\left(\frac{1.9}{5}\right) = 8 \cdot 21.8 = 174.4^\circ \rightarrow 48.44\%$$

where 1.9 is half the width of the C-core, named b in Tab. I and 5 is the radius of the winding.

The material used for the iron is *Soft Iron (With Losses)*. Its relative permittivity is set to 1. Because the iron permeability is unknown, the relative permeability was derived with the help of an RLC meter measurement where the inductance was measured. Moreover, the model was simulated with different permeability until the inductance of the model matched the measurement. The resulting relative permeability was found to be 330. This is the same permeability that is used with (13) in the analytical calculations.

D. Proposed equivalent circuit

This section presents the proposed equivalent circuit and the model's simplifications and assumptions. Additionally, the

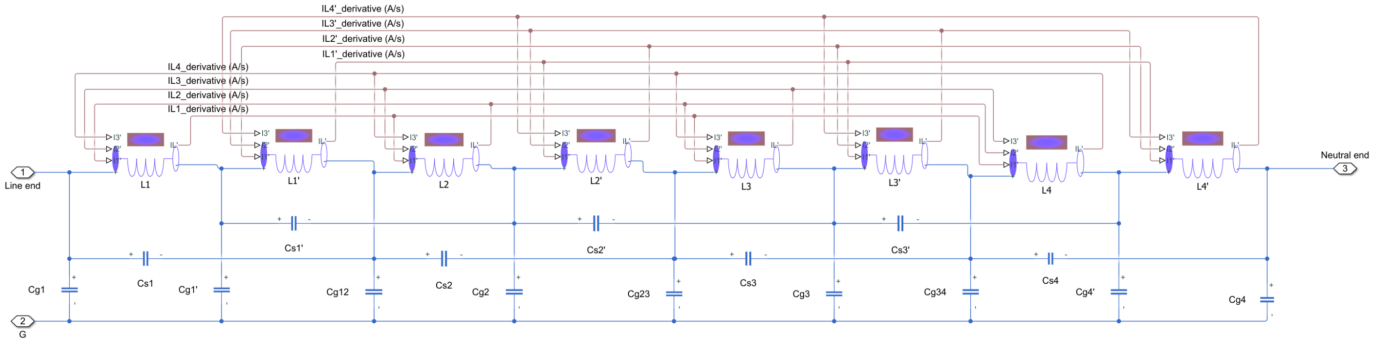


Fig. 11. Proposed equivalent model for simulation of the four turn winding configuration in *Simulink*.

input parameters used in the model are presented for the three winding configurations.

The proposed equivalent circuit for simulations in *MATLAB & Simulink* utilising *Simscape Electrical* represents the turns, or portions of the turns, of the winding as π -equivalents. The model includes series resistance and self-inductance for each turn, with the mutual inductance between turns modelled as in [36]. Additionally, capacitive couplings between turns and ground are included. The model for the four turn winding configuration is shown in Fig. 11. The proposed models for the two and thirteen turn winding configurations are shown in Fig. 25 and Fig. 26 in Appendix B.

Each turn is sectioned into two parts in order to develop a model that accounts for all the travelling waves that might occur during normal operation. Consequently, consisting of four and eight π -equivalents for the two and four turn winding, respectively. The model for the two and four turn winding configuration should be able to predict the created travelling waves for up to rise times $\approx 10ns$ ($f_{max} \approx 100MHz$). On the other hand, the model for the thirteen turn winding configuration should be able to predict the travelling waves for up to rise times $\approx 5ns$ ($f_{max} \approx 200MHz$). The portioning should be fine enough for the study in this thesis since the rise time of the switching devices used in the laboratory experiments is $\approx 50ns$. If switching devices with rise times less than $10ns$ ($5ns$) are to be studied, the travelling wave's wavelength inside the winding is more than 1/10 of the length of one π -equivalent. Hence, each turn should be sectioned even more.

Simplification and assumptions for the model:

- Adjacent turns have significantly higher capacitance than turns that are not adjacent. Therefore, the non-adjacent capacitive couplings are neglected.
- The model cannot catch the frequency dependency of different parameters such as the proximity and skin effects or the effect of the iron. Thus, the model's parameters are calculated for a chosen frequency.
- If the wavelength of the travelling wave inside the winding is more than 1/10 of the length of one π -equivalent, the model is sectioned. The mutual inductance is equally distributed between the π -equivalents. The turn-to-turn

TABLE II
INPUT MODEL PARAMETERS FOR THE SIMULATION OF THE WINDING CONFIGURATIONS IN SIMULINK.

Variable	2 Turn	4 Turn	13 Turn
R_{tb}	$R_t/2$	$R_t/2$	$R_t/3$
R_m	$R_t/2$	$R_t/2$	$R_t/2$
L_{tb}	$L_t/2$	$L_t/2$	$L_t/3$
L_m	$L_t/2$	$L_t/2$	$L_t/2$
$C_{s,tb}$	$C_{s,tb}/4$	$C_{s,tb}/4$	$C_{s,tb}/6$
$C_{s,tb'}$	$C_{s,tb}/2$	$C_{s,tb}/2$	$C_{s,tb}/3$
$C_{s,m}$	$C_{s,m}/2$	$C_{s,m}/2$	$C_{s,m}/2$
$C_{g,tb}$	$C_{g,tb}/4$	$C_{g,tb}/4$	$C_{g,tb}/6$
$C_{g,tb'}$	$C_{g,tb'}/2$	$C_{g,tb'}/2$	$C_{g,tb'}/6 + C_{g,tb'}/4$
$C_{g,tb''}$	$C_{g,tb''}/4 + C_{g,tb''}/4$	$C_{g,tb''}/4 + C_{g,tb''}/4$	$C_{g,tb''}/4 + C_{g,tb''}/4$
$C_{g,m}$	$C_{g,m}/2$	$C_{g,m}/2$	$C_{g,m}/2$

capacitance is divided such that each section of a turn has a connection to its actual adjacent turn section. This is illustrated in the proposed model.

- Parallel conductance is neglected.

1) *Input parameters in the model:* Since the proposed model consists of two π -equivalents per turn, each π -equivalent has half the total parameter value per turn. In Tab. II are the input parameters for the model for each winding presented. It can be observed that the π -equivalent follows a certain pattern. Therefore, the input model parameters are generalised. The subscript *tb* is the first equivalent of the top turn or the last/bottom equivalent of the turn. Subscript *tb'* is the next or the previous equivalent of the first or last turn, respectively (*tb''* for the second next and second last). The subscript *m* represents the parameters of the equivalents in the middle or between *tb*, *tb'* and *tb''*. Finally, the subscript *t* indicates the total turn value of the respective parameter. However, the notation for the turn-to-turn capacitance is subscript *s* and for the turn-to-ground capacitance is subscript *g* used.

E. Impedance frequency response

Here is the experimental setup for the impedance frequency response presented along with a description of the frequency response simulation in *Simulink* and *COMSOL*.

The impedance response of the different winding configurations are tested with a *PSM3750: Frequency response analyzer* with *IAI2 Impedance analyzer* [37] [38]. The impedance frequency response is measured with 50 logarithmic steps from $10Hz$ to $50MHz$. The winding configuration with two and

four turns was tested twice, once without iron and once with iron.

When simulating in *COMSOL*, the *2D Axisymmetric* model with the physics *Magnetic Fields* is used. The impedance is directly extracted from the results of a *Frequency Domain* study. The phase and magnitude of the impedance are found with the command *arg* and *abs*.

When simulating in *Simulink*, the *Time, States and Output* are saved to the workspace in an *Array* format in the *Data Import/Export* section of the *Model Configuration Parameters*. Then, the model is simulated for a specified time with a specified max time step together with an additional block model as shown in Fig. 27 in Appendix C. The code for the simulation and plotting of the impedance response is shown in Appendix C.

F. Experimental setup for the PWM inverter fed windings

This section presents the experimental setup and describes how to conduct the simulation in *Simulink*.

A detailed figure of the experimental setup of the laboratory experiment is shown in Fig. 12. The list below describes each numbered or labelled component in the figure.

- 1) *LÜBCKE VARIO 3R54-220-H*, 0 – 220V, 3x10A
- 2) *3Phase 20kW IGBT Inverter* [39]:
 - DC voltage: 0–640V
 - Switching frequency: 0–25kHz with 0–100% pulse-width modulation
 - Transistors: Semikron SKM400GB125D 2x 400A 1200V IGBT, rise time 50ns, fall time 32ns [40]
- 3) Cable and voltage measurement:
 - Cable: 2m, CATIII, 20A, 1000V.
- 4) Current probe and voltage probe
 - S1: Ch2: *Current probe*, Fluke 80i-110s [42]
 - S1: Ch3: *Voltage probe*, RT-ZP03 [43]
- 5) Cable: 0.2m, CATIII, 20A, 1000V.
- 6) S1: Ch4: *Voltage probe*, RT-ZP03 [43]
- 7) *Winding configuration* with voltage measurements, RT-ZP03, of four turns using all the four channels of Oscilloscope 2 (S2) [43].
- 8) *Measurement reference point*: The S1: Ch3 voltage probe has its ground probe connected at this point.
- 9) *Control unit for the inverter*: PESC control platform
 - Controlled via PC with *WatchView*, see Fig. 28 and Fig. 29 in Appendix D. In *WatchView* is the amplitude of the pure sine wave set for the PWM conversion with unipolar voltage switching. The triangular waveform has a period of 8kHz, and the generated sine wave has a fundamental frequency of 50Hz.
 - Oscilloscope 1 (S1): *R&S RTB2004* [44]
 - Ch1: Voltage measurement of inverter output
 - Ch2: Current measurement

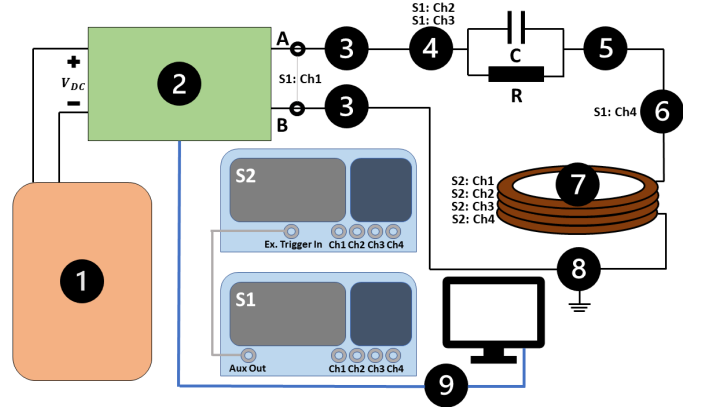


Fig. 12. Experimental setup for the experiment with PWM inverter fed windings.

- Ch3: Voltage across C||R and winding
- Ch4: Voltage across winding
- Aux Out: Trigger signal from Ch1
- Power supply through isolation transformer
- Oscilloscope 2 (S2): *R&S RTB2004* [44]
 - Ch1-Ch4: Turn voltage measurements
 - Ex. Trigger In: Allows for trigger signal in S1 to trigger S2.
 - Power supply through isolation transformer
- R = 1MΩ (Carbon composition)
- C = 0.1μF WIMA KPM 10: 0.1 1600- 10 % A A6 [45]

The resistor in parallel with the capacitor, $R||C$, is introduced to reduce the current without removing the transient effects in the winding. At low frequencies, the voltage will appear mostly across the resistor since $R \gg |Z|$ ($\approx V_{inverter} \cdot \frac{R}{R+Z_{coil}}$). For high frequencies, the capacitive network dominates. Therefore, the high frequency voltage components will appear mostly across the winding, since $X_C \ll X_{C,coil}$ ($\approx V_{inverter} \cdot \frac{X_{C,coil}}{X_{C,coil}+X_C}$).

1) *Simulating the measured voltages*: When simulating in *Simulink*, the measured voltage output from the inverter in the laboratory experiment is directly used in a *Piecewise Linear Voltage Source* block. Its input parameters are two vectors, one for the time and one for the amplitude. Additionally, *Transmission Line* blocks are used for the cables. The input parameters are based on measurements. The block allows for π -equivalents. Thus, the number of equivalents is chosen as described in section II-D. The values in the *Transmission line* block were: 1μH/m, 1pF/m and 0.08Ω/m. In addition, the outgoing wires from the winding configurations are included in the model as lumped DC resistances.

IV. RESULTS

The following sections include the results from the parameter study for the different test objects. Furthermore, the results from the frequency impedance response are presented utilising the results from the parameter study. Finally, the model is simulated and compared against the experiments of

the winding configurations exposed to repeatedly steep fronted voltage surges caused by the inverter. This section will also evaluate and discuss the results.

A. Parameter study

This section presents and discusses the main results and observations from the parameter study. Other results from the parameter study are shown in Appendix E.

1) *Capacitance*: The mutual capacitance matrices for each winding configuration are shown in Tab. VIII, IX and X in Appendix E. The results are collected from these tables and presented in Tab. III for all the different winding configurations and compared against the corresponding capacitance calculated by *COMSOL*. As indicated by the table, are only two-three analytical calculations needed to obtain the matrix for each winding. It can be observed that the turn-to-turn capacitance, C_t , calculations are in good agreement with the capacitance calculated by *COMSOL*. They have a deviation of between 5.5–17.2%. However, the turn-to-ground capacitance has big deviations both for the top and bottom conductor, $C_{g,tb}$, and for the conductors in the middle, $C_{g,m}$. The deviation is 85.4–94.6% compared against *COMSOL*'s calculation. One possible reason for this might be because of the definition of the ground node in *COMSOL* and the ground node in the analytical calculations. Although, the ground node was placed $\approx 0.3m$ from the winding in both the analytical and in *COMSOL*.

The parallel plate approximation only considers an area of the same size as the conductor surface. It does not consider that a charge might find an alternative route across another area that the method does not include. This is probably the reason why the *FEM* calculations give higher capacitance than the analytical calculation. The analytical method struggles, for instance, with calculating the capacitance between conductors that are not adjacent to each other. The resulting calculations would better agree with the turn-to-ground capacitance if the winding were placed in a slot. Placing the ground node closer to the conductors ensures that the area and distance considered in the analytical calculation contribute most significantly to the capacitance. Therefore, the calculation will include most of the charges between the conductor and the ground.

The capacitance is the most crucial parameter to accurately predict in the model because it has the most significant impact on the initial voltage distribution. Therefore, it is essential to know the exact dimensions and insulation material used in the construction of the winding. The insulation material used for the two and four turn windings is uncertain. Only a generalised explanation of the construction of *Isodraht* wires was found,

and it was discovered that the insulation materials used did not include its dielectric properties. Thus, some common properties of the insulation were utilised in the calculations.

Additionally, the two and four turn winding conductors are only glued together. Therefore, the distance between the conductors might be uneven, and there might even be air voids between some parts of the winding. Even though the thirteen turn winding does not fully reflect an actual machine winding because of the distancing of turns and insufficient insulation, the capacitance calculations are much more reliable because there is only air between the conductors and no basecoat nor overcoating on the wires.

2) *Conductance*: The conductance is directly derived from the resulting capacitance. The analytical calculations have not been verified by *COMSOL* or any measurements in the laboratory. Since the parallel conductance is dependent on the permittivity of the insulation and the capacitance, can the values be directly implemented in the *Simulink* model in the block parameters of the capacitor blocks. Since the conductance is not verified and the losses in the insulation materials are small, the conductance has been neglected.

3) *Inductance*: The mutual inductance matrices for each winding configuration are shown in Tab. XI, XII and XIII in Appendix E. The results from the stationary inductance calculations are listed in Tab. IV. All the values are calculated as total inductance for each winding. In the analytical calculations in Tab. IV are (14) and (15) together with (16) used. Additionally, the results from different methods of obtaining the inductance in *COMSOL* are presented in Tab. IV.

All the calculated inductances utilising the *Magnetic Fields* physics in *COMSOL* are in agreement. This is expected since they use the same model to find the inductance. However, the calculated inductances from the *Magnetic Fields, Currents Only* physics deviate slightly. This might be because the model only represents 99.72% of the winding (revolved 2D model 359°). The analytical calculations deviate the most, especially for the thirteen turn winding using (15) and (16).

The mutual coupling factors derived from the mutual inductance matrix extracted from *COMSOL* are listed in Tab. V. Since the matrix is symmetrical is the number of mutual couplings less than the number of turns ($n-1$). Therefore, the mutual couplings are presented as vectors derived from the first row/column of the mutual inductance matrices. These results can be used to calculate the mutual inductance from

TABLE III
COMPARISON OF CAPACITANCE CALCULATED ANALYTICALLY AND WITH THE HELP OF *COMSOL*

Capacitance	2 Turn			4 Turn			13 Turn		
	$C_{g,tb}$	C_t		$C_{g,tb}$	$C_{g,m}$	C_t	$C_{g,tb}$	$C_{g,m}$	C_t
Analytical [pF]	0.33	294.47		0.33	0.16	294.47	0.77	0.18	42.50
COMSOL [pF]	6.15	316.48		5.11	1.66	311.72	5.27	1.44	51.32
Deviation [%]	94.6	7.0		93.5	90.4	5.5	85.4	87.5	17.2

TABLE IV
COMPARISON OF TOTAL COIL INDUCTANCE CALCULATED ANALYTICALLY AND WITH *COMSOL*

Method		2 Turn	4 Turn	13 Turn
(mf): Concentrated flux	[μH]	0.80	2.75	7.55
(mf): Surface integration	[μH]	0.80	2.75	7.55
(mf): Coil inductance	[μH]	0.80	2.75	7.55
(mfco): Coil inductance	[μH]	0.81	2.78	7.57
(Analytical): (14)	[μH]	0.81	2.87	7.98
(Analytical): (15), (16)	[μH]	0.83	2.79	12.99

TABLE V
EXTRACTED MUTUAL COUPLING FACTOR OF THE INDUCTANCE MATRIX
CALCULATED BY *COMSOL*.

Coupling factor	[M]											
2 Turn	[0.81]											
4 Turn	0.81	0.64	0.53									
13 Turn	0.71	0.51	0.38	0.28	0.22	0.17	0.14	0.11	0.09	0.07	0.06	0.05

the total inductance of the winding with the help of (33).

The frequency-dependent analytical calculations are compared against the *2D Axisymmetric* models in *COMSOL*. When simulated without iron, the skin effects can be investigated. Fig. 13 plots the calculated inductance with skin effects for the four turn winding ($L_t = L_{ins} + \Im(Z_{sk}) \cdot l$). It is indicated by *COMSOL* that the inductance is slightly reduced from its stationary value, $2.75\mu H$, to $\approx 2.48\mu H$ at $100MHz$. The same observation can be made from the analytical calculation. Here, the inductance is reduced from $2.79\mu H$ to $2.65\mu H$ at $10kHz$. After this frequency, the inductance is reduced significantly faster than what was predicted by *COMSOL*.

When simulated with iron, the effects of iron can be investigated. It can be observed from the *COMSOL* simulation that the skin effect does not change the inductance significantly before after $30MHz - 50MHz$. Before such high frequencies, the inductance is slightly reduced, similarly as in Fig. 13. The inductance varies around its stationary value without the iron present for higher frequencies.

When the effects of the iron is investigated analytically, the skin effects were not included, since it has already been studied in Fig. 13 ($L_t = L_{ins} + L_{iron} \cdot l$). It is observed from Fig. 14 that the term calculating the effects of iron is fast reduced to zero. However, the deviation between them is $\approx 8\mu H$ for the lowest frequency.

When inductance formulas were selected, several methods were studied before settling for two approaches, both of which gave reasonable estimations compared with the *COM-*

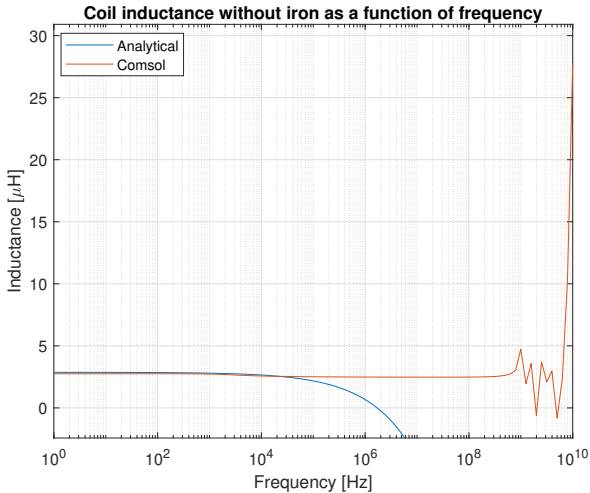


Fig. 13. Calculated inductance frequency dependency for the four turn winding without iron.

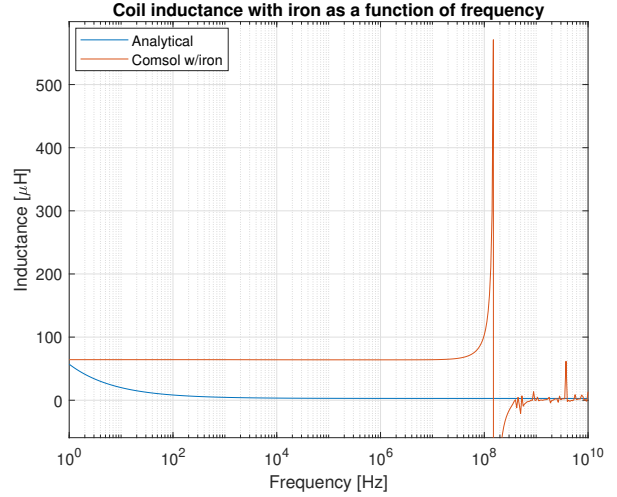


Fig. 14. Calculated inductance frequency dependency for the four turn winding with iron.

SOL models. The analytical formula calculating the mutual inductance and self-inductance, (15) and (16), are the most complicated of the analytical calculations. Whether these two formulas were used correctly is still unsure to the author because it is observed to deviate more from the other methods for the thirteen turn winding configuration, see Tab. IV and Tab. X. The problem might be that the method is not valid for such big conductor cross-sections. Alternatively, the user might have partially utilised the method correctly but failed to divide the rectangular cross-sections into several small square cross-sections. This mistake may not introduce significant errors before the sections become more than two.

Regarding the frequency-dependent analytical calculations, it should be noted that they have only been used for lower frequency ranges than what this thesis has studied. For instance, (13) and (19) were only used for frequencies up to $200kHz$ in [26]. This could explain the deviations between the calculated and the simulated parameters, although user errors for the analytical calculations or modelling errors can not be ruled out either.

4) *Resistance*: The DC resistance for each turn has been calculated and presented in Tab. VI. When comparing the two methods together, it can be observed that they differ $\pm 1\mu\Omega$. This insignificant difference is expected since the frequency-independent analytical approach is based on the same DC calculation as the *FEM* uses, (27), and the results from these calculations are therefore in good agreement.

The behaviour of the resistance as a function of frequency

TABLE VI
CALCULATED DC RESISTANCE PER TURN FOR THE DIFFERENT WINDING CONFIGURATIONS.

Resistance, R_t	2 Turn [$m\Omega$]	4 Turn [$m\Omega$]	13 Turn [$m\Omega$]
Analytical	0.308	0.308	0.076
<i>COMSOL</i>	0.309	0.309	0.075

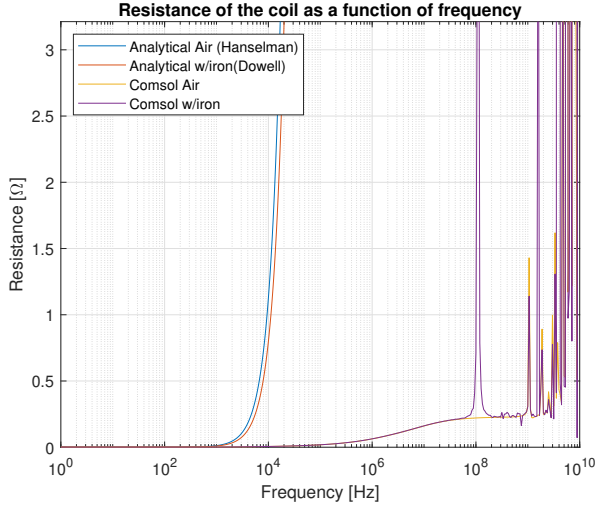


Fig. 15. Calculated resistance frequency dependency for the four turn winding for plotted both with and without iron.

has been plotted in Fig. 15. It includes the resistance both without and with iron, Dowell’s formula (23) and Hanselman’s (30) formula, respectively. They are plotted against the resistance extracted from the *2D Axisymmetric* model. It can be observed from the model that the analytical calculations accurately predict the resistances up to a few hundred Hz . Then, the resistance increases significantly faster than what was predicted by *COMSOL*. Somewhat similar behaviour is predicted by *COMSOL* for frequencies above $1MHz$.

In the frequency-dependent formulas is the increase of resistance caused by skin effects, proximity effects and the effects of the iron deviating from the behaviour of the resistance using *FEM* in *COMSOL*. This might be because in most cases where the resistance has been studied, it has not been considered for frequencies above MHz ranges. The analytical and *FEM* calculated resistances are in good agreement with each other for low frequencies. Another interesting observation from the *FEM* simulation is that the resistance seems to have more or less the same behaviour regardless of whether the iron is present or not. However, the *FEM* calculations gave “spikes” and considerable variations in the resistance for very high frequencies above $100MHz$. The reason for this observation is probably connected to the method *COMSOL* utilised to include the losses introduced by the iron. By only including the relative permeability in the model is a linear relationship between the **B**-field and the **H**-field used in the simulation. Hence, this approach is inaccurate because the material might experience saturation, which is not detected by the linear relationship. A more accurate and realistic model approach would have been to utilise the non-linear relationship with the help of a **BH**-curve.

B. Frequency impedance response

This section presents the frequency response of the four turn winding configuration in Fig. 16. There are a total

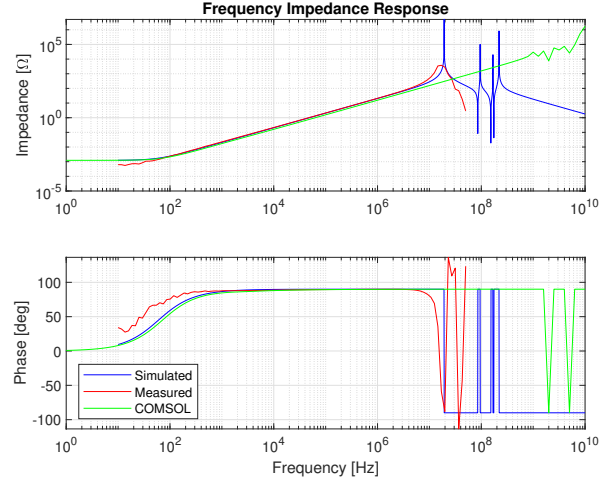


Fig. 16. Frequency impedance response of the four turn winding without iron.

of five different measured frequency impedance responses. Their observed resonance points are presented in Tab. VII. The plots of the impedance responses for the other winding configurations are presented in Fig. 30, Fig. 31, Fig. 32 and Fig. 33 in Appendix F.

In Tab. VII, the first resonance point, first antiresonance point, and second resonance point are listed for the measurements and the simulated results from the proposed model. It can be observed that both the impedance amplitude and phase are in agreement for the simulations and measurements, however, only before the occurrence of resonance points. The simulations conducted in *COMSOL* are not able to predict the resonance points because they are observed to appear at too high frequencies compared with the measurements. Nevertheless, for lower frequencies, the impedance amplitude and phase are almost identical to the predictions of the *Simulink* model.

It can also be observed, especially for the thirteen turn wind-

TABLE VII
OBSERVED RESONANCE POINTS FOR MEASUREMENTS AND SIMULATIONS IN SIMULINK.

Resonance	1st [MHz]	1st' [MHz]	2nd [MHz]
Two turn winding (Air)			
Measured	19.82	33.98	-
Simulated	33.97	150.61	215.28
Two turn winding (Iron)			
Measured	19.82	26.98	-
Simulated	10.61	47.03	67.24
Four turn winding (Air)			
Measured	16.96	19.82	31.49
Simulated	19.22	85.55	94.91
Four turn winding (Iron)			
Measured	10.69	19.82	36.73
Simulated	3.98	17.70	19.63
Thirteen turn winding			
Measured	7.86	14.56	16.99
Simulated	42.11	101.04	106.02

ing configuration, that the *Simulink* model struggles at higher frequencies. It should be noted that the models are not valid for frequencies higher than 100MHz (200MHz for the thirteen turn winding configuration). However, it was simulated for higher frequencies to see the comparison between the model and *COMSOL* simulations.

The proposed models in *MATLAB & Simulink* simulated the impedance responses with 10^5 logarithmic steps from 10Hz to 10GHz . Since the model cannot include the frequency-dependent variables from the parameter study, the model used different DC values. The values utilised are already calculated for each winding for the case where the iron is not included. The derived mutual coupling factors are the same as the ones listed in Tab. V. The self-inductance used in the simulation is the extracted total coil inductance from the *2D Axisymmetric* models. The total inductance is solved for L in (33). When including iron in the simulation, only the inductance was changed to its DC value. The total coil inductance with the C-cores for the two turn and four turn winding is found to be $8.2\mu\text{H}$ and $64.3\mu\text{H}$, respectively.

Even though the model uses DC values for its parameters, it was observed that the models could include the frequency-dependency by itself. If this holds for all coils, the analytical calculations are significantly simplified. The inductance was increased to account for the effect of the iron, which caused the resonance point to arrive earlier. Similarly, increasing the turn-to-turn and turn-to-ground capacitance in the case of better insulation will cause the resonance points to arrive earlier as well, which is expected from (3).

The performance of the frequency analyser, PSM3750, is less accurate for high frequencies. However, the model simulations have shown that the impedance response measured is not necessarily inaccurate. The predicted first resonance, first antiresonance and second resonance points are in good agreement for the two and four turn winding without the iron present, strengthening the faith in the proposed model.

Since *COMSOL*'s resonance points were not in agreement with either the proposed model or the measurements raises questions about whether the software was utilised correctly for the impedance response. However, the impedance amplitudes and phases agree with the proposed model before the occurrence of resonance points. Since the development of the proposed models and the *COMSOL* models are only based on exact geometric dimensions, they are more similar to each other than the actual test object. Hence, strengthening the faith in the model even further. On the other hand, the actual test object includes other uncertainties not included in the models, e.g. cables, poor probe connections, and other disturbances.

C. PWM inverter fed winding

In this section, the results from the simulations and laboratory experiments are presented for the case where the winding is exposed to surge voltages caused by the inverter. The setup of the experiment is as described in section III-F.

1) *Inverter operation*: The measured no-load voltage of the inverter is plotted in Fig. 17. With an amplitude of

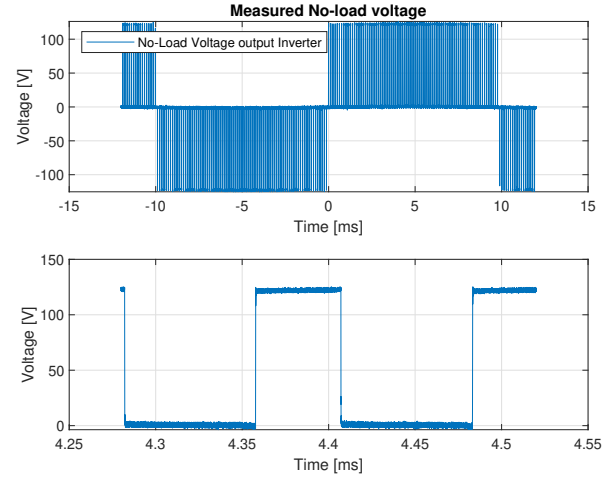


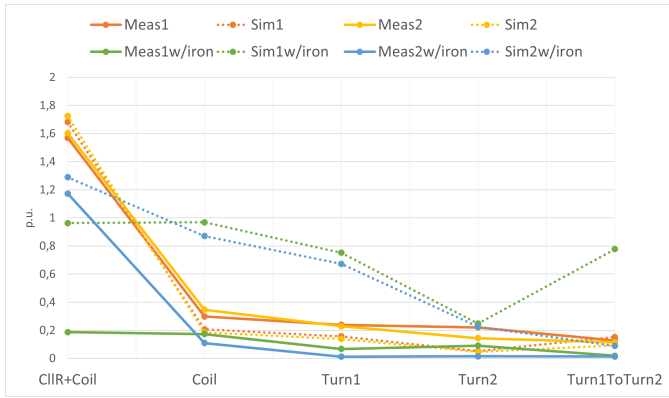
Fig. 17. A full period and a closer snapshot of the No-Load voltage output of the inverter.

120V , the rise time is measured to be 20ns – 60ns ($dV/dt = 1600\text{V}/\mu\text{s}$ – $4800\text{V}/\mu\text{s}$), and the fall time is measured to be 60ns . Additionally, a tilt of approximately 4% and an overshoot equal to 4% are observed.

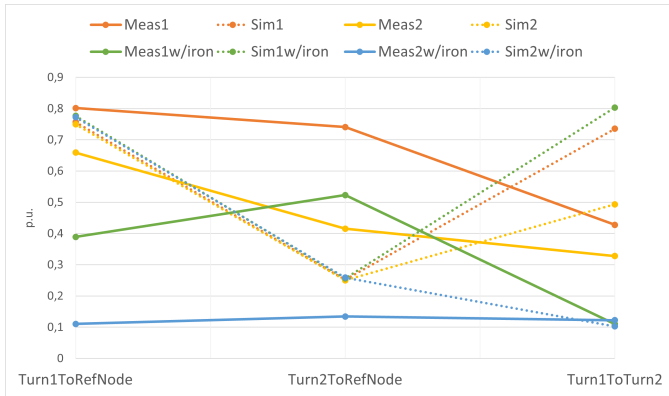
The gate trigger signals $A+$ and $B+$ have been measured to make sure that the inverter operates as intended. It can be observed from Fig. 34 in Appendix G that the resulting square wave voltages are generated as expected.

2) *Measured and simulated results*: Some of the measured and simulated voltage waveforms are plotted and presented in Appendix G. Including every simulation and measurement will occupy too much space. Thus, only half of the laboratory measurements are plotted with their corresponding simulated results. The model's performance is measured in the accuracy of the worst predicted voltages between turns and between the turns and the ground reference. The simulated models have been expanded to include the probes' effects by connecting the impedance between the measurement and ground reference points. The impedance for the RT-ZP03 probe is $10\text{M}\Omega$ in parallel with 12pF [43].

The experiments consist of measurements and simulations with two voltage levels on the DC-link. Fig. 18, Fig. 19 and Fig. 20 are label *Meas1/Sim1* and *Meas2/Sim2* indicating the the measured or simulated result with DC-link voltage level $\approx 100\text{V}$ or $\approx 185\text{V}$, respectively. In addition, the two and four turn windings were tested with the C-cores. In Fig. 18 and Fig. 19 is the additional label *w/iron* indicating the test with iron present. The highest measured voltage of each probe has been collected from the results. The data are divided by the measured/simulated inverter voltage to compare the simulated and the measured voltages. It was observed that the model, in some cases, gave too high/low voltage across the coil. This might indicate that the modelling of the cables or the $R||C$ component is wrong. Another comparison was created to compensate for these errors. The simulated data was divided by the simulated coil voltages, and the measured data was



(a) Simulated and measured voltages for the two turn winding with inverter voltage as reference.

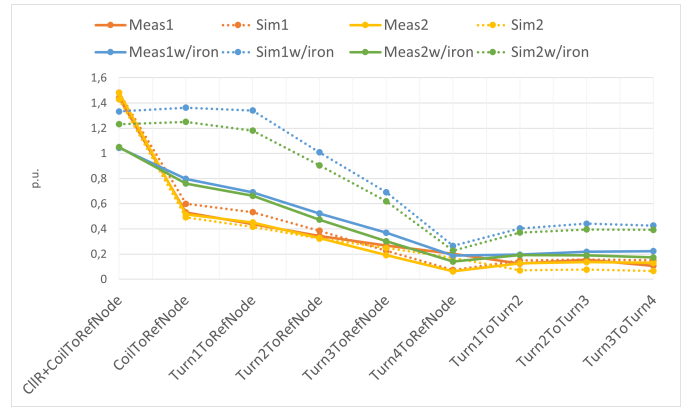


(b) Simulated and measured voltages for the two turn winding with coil voltage as reference.

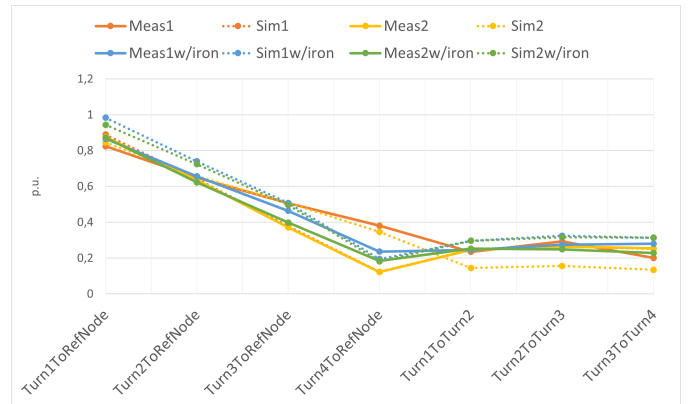
Fig. 18. Comparison of measured and simulated per unit voltages for the two turn winding.

divided by the measured coil voltages. The results from both approaches for the comparisons are shown in Fig. 18, Fig. 19 and Fig. 20.

From Fig. 18(a) it is observed that the simulated and the measured voltages for the two turn winding are in good agreement without the iron present. The simulated turn voltages are slightly less than the measured ones, at most 16.9%. However, the predicted worst turn-to-turn voltage is less than 2.5% off. Moreover, it is observed that when the iron is introduced, the voltages are not in agreement. This indicates that using the calculated DC inductance that includes iron in the lumped equivalent model does not give accurate results. From Fig. 18(b) it is observed that the simulated results give consistent turn voltages distribution. However, the predicted turn-to-turn voltages or the measured voltages are not in agreement. It is unclear why the observed simulated and measured voltages with the coil voltage as reference are so different. A possible explanation is that the actual two turn winding is the least ideal constructed windings because it was the most challenging winding to obtain good probe connections with turns. Another possible explanation is that the glue had failed to keep the turns together, causing the turns to be slightly



(a) Simulated and measured voltages for the four turn winding with inverter voltage as reference.



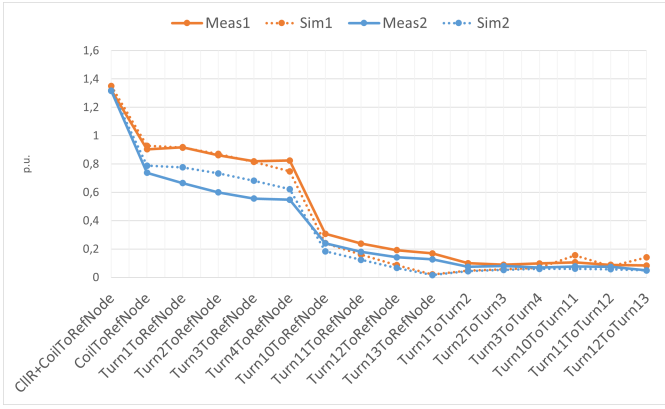
(b) Simulated and measured voltages for the four turn winding with coil voltage as reference.

Fig. 19. Comparison of measured and simulated per unit voltages for the four turn winding.

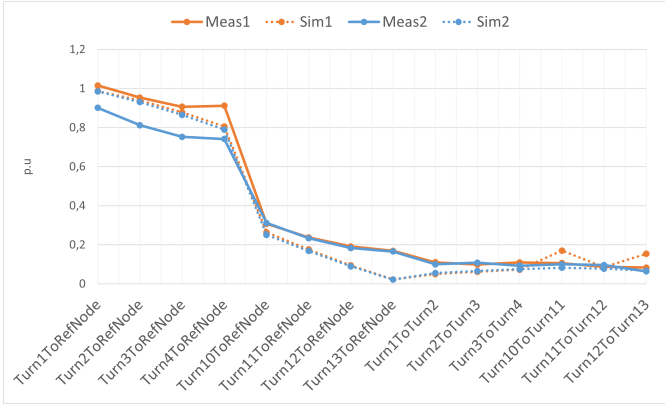
unwound, which will affect the capacitive couplings.

The simulations and measurements for the four turn winding show that the model accurately predicts the voltage distribution without the iron present. Fig. 19(a) and Fig. 19(b) show clearly that the coil acts as a voltage divider and that the predicted turn-to-turn voltages are almost equal. The precision of the predictions of the turn voltages is between 0.4% and 12.8%. The voltage distributions are also quite accurately predicted when using the voltages across the coils as base values. The voltages for turn four have the worst precision with the test where the inverter voltage was $\approx 100V$.

The thirteen turn winding was only tested as air coils. The simulated and measured voltage distribution is in good agreement using both approaches of comparison, as seen in Fig. 20(a) and Fig. 20(b). It is observed that the model tends to underestimate the highest turn-to-turn voltages, although the accuracy is only deviating 7% at the most. The measured and simulated turn-to-turn voltages are almost equal, although it can be observed that the appearing turn-to-turn voltages are slightly higher between the last turns. The differences between the simulated and the measured voltages are not significant.



(a) Simulated and measured voltages for the thirteen turn winding with inverter voltage as reference.



(b) Simulated and measured voltages for the thirteen turn winding with coil voltage as reference.

Fig. 20. Comparison of measured and simulated per unit voltages for the thirteen turn winding.

Hence, strengthening the faith in the proposed model even further.

V. DISCUSSION

In this section, the model choices and the experimental setup is discussed. The methods and approaches used in *COMSOL*, the analytical parts and modelling will be evaluated. Then, the section concludes with a reflection on the validity of the results of the proposed model for voltage distribution predictions.

A. Parameter study

Throughout the literature study, it was discovered that there are many suggested methods for analytically calculating the parameters of different kinds of winding configurations. In particular, there are many inductance formulas. Therefore, the parameter study targeted formulas for cylindrical coils or similar methods used in studies of the same subject. Typical winding configurations used in electrical machines are not cylindrical. Consequently, the analytical parts of this thesis might not be able to predict parameter values for other types of winding configurations accurately. This applies especially to the calculation of inductance.

B. COMSOL model

When modelling in 3D, one might encounter the problem that the layer thicknesses are too thin. A finer mesh can be used in some cases where the minimum layer thickness is not violated. If the layer thickness is less than the minimum layer thickness, the mesh gives the warning: *Domain has a region that is much thinner than the specified minimum element size*. Introducing a *Thin low permeability gap* or similar *Boundary layer* features can solve the problem [35]. However, this problem was avoided by using the *2D Axisymmetric* model.

The C-ferrite cores in both the *COMSOL* and the *Simulink* models are heavily based on a *RLC* meter measurement. Hence, the iron's permeability in the model was found by trying different properties until an equal inductance was obtained. Dividing the two components into parts, with and without iron, and adding them together to include the effects of iron might not be the best approach either. A better approach, but probably with much slower computation time, is to use a 3D model.

The behaviour of the voltage distribution in the experiment indicated that the inductance and resistance had different values than the models used in the simulations. What component in the model that in reality has another value is hard to tell, although the cables using transmission line blocks has the highest uncertainty. Alternatively, it simply suggests that the model cannot use the DC values and that the parameters should be calculated for a given frequency, possibly the switching or oscillation frequency.

C. PWM inverter fed winding

1) *Laboratory setup*: As mentioned in section III-F was the $1M\Omega$ in parallel with the capacitance of $0.1\mu F$ introduced such that the inverter would be able to conduct the experiments without too high currents. Much time was spent trying to find a neatly arranged solution for how the measurements could be realised without introducing too many unknowns/uncertainties to the proposed *Simulink* model. At the beginning of the work, the laboratory experiment aimed to find a solution to mimic a real machine. A real machine will have its coils placed inside slots, resulting in higher total inductance of the coils than coils mounted in the air without the iron present. Therefore, the C-core was introduced as an attempt to increase the inductance. If the inductance is too low, the current will be too high to carry out experimentation in the laboratory. In real machines, the back emf is caused by opposing the rotor's magnetic field, which results in a lower current through the coils in the stator.

At first, when the motor is turned on, the winding receives the full driving voltage. According to Lenz's law, the back emf grows as the motor turns faster. The law states that the direction of current induced in a conductor by a changing magnetic field, as per Faraday's law, is such that the magnetic field created by the induced current opposes the initial changing magnetic field which produced it [30]. One idea was that a secondary coil could be placed such that the two coils shared their magnetic circuit and that this would make it possible to reduce the current in the coil. The secondary coil could create

a magnetic field in the opposite direction of the exited coil, and this would cause the magnetic field to vary as a function of the current induced in the secondary coil. The variation in the magnetic field would result in a back emf in the exited coil, reducing the current through the coil. This approach was tested, both for a separately excited secondary coil and for a passive short-circuited coil. Still, the tests showed that the inductance was too low to carry out the experiments. The voltage was observed to collapse during each applied square wave.

The voltage probes in the setup need to be correctly adjusted for both low and high frequencies for the measurements to be reliable. Furthermore, a good connection between the copper and the probe is essential for a suitable measurement. Establishing sufficient connections to a turn was not always easy for the windings with the tiniest wires, meaning the two and four turn winding configuration. The measurement points can be seen in Fig. 21 and Fig. 22. Before new coils are wound for further investigations and experiments in the future, this should be considered. The measurement points are also not ideally located, such that the measured turn voltages are either for more than a complete turn or less than a complete turn. However, the turns in the proposed model are modelled as complete turns, which might explain some of the observed deviations from the voltage waveforms.

Watchview was used as a control platform for the inverter. The amplitude reference was set to four and kept at this level for all tests to prevent the occurrence of overvoltages. The resulting sine waveforms are shown in red and green in Fig. 29 in Appendix D. When setting the value while in operation, the user should ensure that the value inserted does not cause overmodulation because of a typing error. This can cause more side-band harmonics, and linear operation is therefore preferred in this study [13].

The full potential output voltage of the inverter was not utilised due to a problem with the oscilloscope and probes. The probes cannot handle transient with higher peak voltages than 600V, which potentially would occur across the resistance in parallel with the capacitance and the coil. Additionally, the oscilloscope would not allow displaying voltages higher than $\pm 250V$. Moreover, higher applied voltages might cause too high currents, above 20A, damaging the setup's cables. For these reasons, a higher voltage test was not conducted even though medium voltages were the aim at the beginning of the work.

When two oscilloscopes were used simultaneously, a delay between the measurements was detected. The delay can be seen in Fig. 35(b) and Fig. 35(d) in Appendix G. The delay varied slightly from measurement to measurement. Hence, all the turn voltages were measured by the same oscilloscope. Therefore, the delay would not introduce errors in the resulting amplitudes and oscillations when the turn-to-turn voltages were investigated. When plotting the voltage waveforms, the delay was manually measured in *MATLAB*, and the measured data was given a time offset. Therefore, the timing of the turn voltages might not represent the actual timing of the response.

2) *Simulations in Simulink*: Since the results from the impedance response indicated that using stationary values in the model would be correct, the model was simulated with stationary values. It was observed that increasing the inductance to include the effects of the iron caused higher overvoltages than what was measured. Additionally, the frequency of oscillation would change. Different values showed that the voltage distribution with iron present would have less inductance than the inductance used in the simulation and higher resistance to damp the oscillations. However, there was no method of finding the correct values that made sense from the parameter study. The results from *COMSOL* helped observe whether any of the predicted parameter values would accurately predict the voltage distribution. Settling for using the predicted parameters for the air coils would surprisingly be more accurate, as seen by Fig. 18(a) and Fig. 19(a). The reason for this could be explained by observing *COMSOLs* predicted behaviour of the inductance when the iron is present, Fig. 14. In this figure, the inductance was observed to drop to approximately the inductance value without the iron. This observation is supported by the impedance responses listed in Tab. VII. The measured resonance points that have been affected by the introduction of iron appear to arrive some *MHz* earlier, but not as significantly early as when stimulated with DC calculated inductance. This indicates that the inductance should have been slightly higher than the air coils in the simulations. Additionally, it indicates that the relative permeability of the iron approaches unity at sufficiently high frequencies.

Regarding the *Model settings* in *Simulink*, it is important to stress that choosing the right settings is very important for the performance of the model. There is a *Global* and *Local* model setting in *Simscape Electrical*. In the *Global* model setting, the solver *ode23tb* is selected, and in the *Local* model setting, the solver type *Backward Euler* with a sample time equal *1ns* is selected. Increasing the sample time will lower the simulation time. However, the model might no longer be able to catch the transient effects.

The model was simulated with the inverter output voltages applied to the winding to validate the proposed model. The results from both the simulations and measurements indicate that the voltages are evenly distributed among the turns. Additionally, the turn-to-turn voltages are almost equal. However, the impact of the cables, the *R||C* component, the iron and the material properties introduced new uncertainties to the model. By examining the measured and simulated plots in Appendix G, it is clear that the model gave the most accurate response for the thirteen turn winding, which are the parameters that are calculated with the highest confidence of the three windings.

VI. CONCLUSION

In this thesis, a method of developing a *Lumped equivalent circuit model* has been presented. The model uses π -equivalents representing portions of the winding. The corresponding length of each portion is less than 1/10 of the

length of the travelling waves that might occur during normal operation of the inverter. The π -equivalents consist of series resistance, self-inductance, mutual inductance, turn-to-turn capacitance and turn-to-ground capacitance. A comparison of an analytical approach and a *FEM* based approach to determine the parameters has also been presented. The analytical calculated stationary parameters were in good agreement with the simulation software *COMSOL Multiphysics*[®]. *COMSOL* has proven to be a powerful tool for obtaining the parameters of the winding. Regardless, an experienced user is without a doubt needed for a confident appliance of the software.

The proposed *Simulink* model was validated using two different experimental approaches and three different winding configurations. The first experiment measured the frequency impedance response for each winding configuration. Then, the measurements were compared with the simulated response. It was observed that the simulations and measurements were in good agreement for the two and four turn winding. However, it was demonstrated that the introduction of the iron increased the inductance, which caused the resonance points to arrive earlier. Additionally, it was observed that the model struggles to predict responses for frequencies above the model's capabilities, $\approx 100\text{MHz}$ – 200MHz . The predicted frequency responses from the *COMSOL* model were not in agreement with either the measured or simulated impedance response.

The last experiment utilised pure sine wave conversion for a unipolar PWM operated inverter. The testing consisted of two voltage levels, one with $\approx 100\text{V}$ and a second with $\approx 185\text{V}$. The rise times of the generated square waves were observed to be 20ns – 60ns . The simulated results gave a reasonable degree of confidence in the proposed model and its capabilities to predict the voltage distribution in the winding. Although, further testing and investigations are required for the model to be valid in more complex contexts. So far, the experiments have shown that using the inductance value for the case of an air coil gave voltage predictions closest to the measured voltage distribution with and without the iron present.

VII. FURTHER WORK

- Investigations of winding configurations where not all turns are placed on top of each other. For example, having an eight turn winding where four turns are placed on top of each other in parallel with the following four turns placed on top of each other. In this way, the travelling wave will arrive later for the adjacent parallel turns. Hence, the measured turn-to-turn voltages (turn1-to-turn5, turn2-to-turn6...) will differ from this study.
- Develop a *Multiconductor transmission line model* for machine windings. This model is considered more accurate and able to include frequency dependency of parameters. Furthermore, investigate if the *MATLAB* command *linmod* of the proposed model can be used in the *MTLT* directly. If this is possible, the two different approaches can be compared and validated.

- Continue laboratory experiments aiming to get closer to a real machine's setup and find solutions to how the model must be developed.
 - Including a full phase or even three phases.
 - Including rotating magnetic fields.
 - Including a stator with windings inserted in slots.
- Develop and compare against similar models, e.g. utilising *Simscape Electrical Specialized Power Systems* or other transient simulation programs. This will reveal if there are easier or more accurate programs that can be used or if the utilisation of *Simulink* is sufficient.

ACKNOWLEDGMENT

The author would like to thank supervisors Pål Keim Olsen at NTNU and Njål Rotevatn and Viljar Fjellanger at Rolls-Royce Electrical Norway AS for their guidance throughout the thesis's work. Their help and fruitful discussions have been most appreciated. In addition, the author would like to express gratitude to the workshop for constructing two of the windings, to the service lab and to Thomas S. Haugan at NTNU for the help with the laboratory setup. Furthermore, the author is grateful to have had the opportunity to borrow the frequency analyser from Rolls-Royce Electrical Norway AS.

REFERENCES

- [1] J. Benzaquen, J. He, and B. Mirafzal, "Toward more electric powertrains in aircraft: Technical challenges and advancements," *CES Transactions on Electrical Machines and Systems*, vol. 5, no. 3, pp. 177–193, Sep. 2021, conference Name: CES Transactions on Electrical Machines and Systems.
- [2] S. Sahoo, X. Zhao, and K. Kyprianidis, "A Review of Concepts, Benefits, and Challenges for Future Electrical Propulsion-Based Aircraft," *Aerospace*, vol. 7, no. 4, 2020. [Online]. Available: <https://www.mdpi.com/2226-4310/7/4/44>
- [3] A. Barzkar and M. Ghassemi, "Electric Power Systems in More and All Electric Aircraft: A Review," *IEEE Access*, vol. 8, pp. 169 314–169 332, 2020, conference Name: IEEE Access.
- [4] T. Humiston and P. Pillay, "Parameter measurements to study surge propagation in induction machines," *IEEE Transactions on Industry Applications*, vol. 40, no. 5, pp. 1341–1348, Sep. 2004, conference Name: IEEE Transactions on Industry Applications.
- [5] G. Lupo, C. Petrarca, M. Vitelli, and V. Tucci, "Multiconductor transmission line analysis of steep-front surges in machine windings," *IEEE Transactions on Dielectrics and Electrical Insulation*, vol. 9, no. 3, pp. 467–478, Jun. 2002, conference Name: IEEE Transactions on Dielectrics and Electrical Insulation.
- [6] V. Mihaila, S. Duchesne, D. Roger, and P. Y. Liegeois, "Prediction of the turn-to-turn voltages in parallel connected wires configuration for motor coils fed by steep fronted pulses," in *2011 Electrical Insulation Conference (EIC)*, Jun. 2011, pp. 407–412, iSSN: 2334-0975.
- [7] L. Gubbala, A. von Jouanne, P. Enjeti, C. Singh, and H. Toliyat, "Voltage distribution in the windings of an AC motor subjected to high dV/dt PWM voltages," in *Proceedings of PESC '95 - Power Electronics Specialist Conference*, vol. 1, Jun. 1995, pp. 579–585 vol.1.
- [8] F. Perisse, P. Werynski, and D. Roger, "A New Method for AC Machine Turn Insulation Diagnostic Based on High Frequency Resonances," *IEEE Transactions on Dielectrics and Electrical Insulation*, vol. 14, no. 5, pp. 1308–1315, Oct. 2007, conference Name: IEEE Transactions on Dielectrics and Electrical Insulation.
- [9] C. Zheng, Q. Wang, H. Wang, C. L. Bak, and Z. Shen, "Uneven Inter-turn Voltage Distribution among Windings of Medium-voltage Medium/High-frequency Transformers," in *2020 IEEE International Conference on High Voltage Engineering and Application (ICHVE)*, Sep. 2020, pp. 1–4, iSSN: 2474-3852.

- [10] W. Jianru, L. Hongchi, and Y. Huajun, "Voltage distribution in stator windings of the motor driven by PWM inverter," in *Proceedings. International Conference on Power System Technology*, vol. 2, Oct. 2002, pp. 727–731 vol.2.
- [11] R. S. Ferreira and A. C. Ferreira, "Three-Phase Model for Studying Turn-to-Turn Transient Voltage Distribution in Rotating Machine Stator Windings," in *2021 IEEE Electrical Insulation Conference (EIC)*, Jun. 2021, pp. 47–51, iSSN: 2576-6791.
- [12] A. Misra, "Energy Storage for Electrified Aircraft: The Need for Better Batteries, Fuel Cells, and Supercapacitors," *IEEE Electrification Magazine*, vol. 6, no. 3, pp. 54–61, Sep. 2018, conference Name: IEEE Electrification Magazine.
- [13] N. Mohan, T. M. Undeland, and W. P. Robbins, *Power Electronics: Converters, Applications, and Design*, 3rd ed. United States of America: John Wiley & Sons, Inc., 2003.
- [14] ABB, "IGBT Cosmic Ray Capability, APPLICATION NOTE 5SYA 2042-09," 2019.
- [15] M. Rahimo, "Performance Evaluation and Expected Challenges of Silicon Carbide Power MOSFETs for High Voltage Applications," *Materials Science Forum*, vol. 897, pp. 649–654, May 2017. [Online]. Available: <https://www.scientific.net/MSF.897.649>
- [16] K. Ni, Y. Liu, Z. Mei, T. Wu, Y. Hu, H. Wen, and Y. Wang, "Electrical and Electronic Technologies in More-Electric Aircraft: A Review," *IEEE Access*, vol. 7, pp. 76 145–76 166, 2019, conference Name: IEEE Access.
- [17] R. Kerkman, D. Leggate, and G. Skibinski, "Interaction of drive modulation and cable parameters on AC motor transients," in *IAS '96. Conference Record of the 1996 IEEE Industry Applications Conference Thirty-First IAS Annual Meeting*, vol. 1, Oct. 1996, pp. 143–152 vol.1, iSSN: 0197-2618.
- [18] S. Kulkarni, "Transformer engineering : design and practice," 2004, iISBN: 0824756533 Place: New York Series: Power engineering Volume: 25.
- [19] D. D'Amato, J. Loncarski, V. G. Monopoli, F. Cupertino, L. P. Di Noia, and A. Del Pizzo, "Impact of PWM Voltage Waveforms in High-Speed Drives: A Survey on High-Frequency Motor Models and Partial Discharge Phenomenon," *Energies*, vol. 15, no. 4, p. 1406, Jan. 2022, number: 4 Publisher: Multidisciplinary Digital Publishing Institute. [Online]. Available: <https://www.mdpi.com/1996-1073/15/4/1406>
- [20] "Rotating electrical machines - Part 18-41: Partial discharge free electrical insulation systems (Type I) used in rotating electrical machines fed from voltage converters - Qualification and quality control tests," IEC 60034-18-41, Tech. Rep., Jun. 2019.
- [21] S. Ma, J. Guo, H. Sun, and Y. Yu, "The comparison and analysis of lumped parameter equivalent circuits of transmission line," in *2011 International Conference on Advanced Power System Automation and Protection*, vol. 2, Oct. 2011, pp. 1225–1229.
- [22] A. Krings, G. Paulsson, F. Sahlén, and B. Holmgren, "Experimental investigation of the voltage distribution in form wound windings of large AC machines due to fast transients," in *2016 XXII International Conference on Electrical Machines (ICEM)*, Sep. 2016, pp. 1700–1706.
- [23] O. Magdun, S. Blatt, and A. Binder, "Calculation of stator winding parameters to predict the voltage distributions in inverter fed AC machines," in *2013 9th IEEE International Symposium on Diagnostics for Electric Machines, Power Electronics and Drives (SDEMPED)*, Aug. 2013, pp. 447–453.
- [24] J. Faria, "Capacitor modeling at high frequencies-a pedagogical example of the application of distributed circuit analysis for introductory electromagnetics or microwave courses," *IEEE Transactions on Education*, vol. 35, no. 3, pp. 214–216, Aug. 1992, conference Name: IEEE Transactions on Education.
- [25] M. Popov, L. van der Sluis, R. P. P. Smeets, and J. Lopez Roldan, "Analysis of Very Fast Transients in Layer-Type Transformer Windings," *IEEE Transactions on Power Delivery*, vol. 22, no. 1, pp. 238–247, Jan. 2007, conference Name: IEEE Transactions on Power Delivery.
- [26] J. Guardado, J. Flores, V. Venegas, J. Naredo, and F. Uribe, "A machine winding model for switching transient studies using network synthesis," *IEEE Transactions on Energy Conversion*, vol. 20, no. 2, pp. 322–328, Jun. 2005, conference Name: IEEE Transactions on Energy Conversion.
- [27] H. Wheeler, "Simple Inductance Formulas for Radio Coils," *Proceedings of the Institute of Radio Engineers*, vol. 16, no. 10, pp. 1398–1400, Oct. 1928, conference Name: Proceedings of the Institute of Radio Engineers.
- [28] K. Wirgau, "Inductance calculation of an air-core disk winding," *IEEE Transactions on Power Apparatus and Systems*, vol. 95, no. 1, pp. 394–400, Jan. 1976, conference Name: IEEE Transactions on Power Apparatus and Systems.
- [29] J. Guardado and K. Cornick, "A computer model for calculating steep-fronted surge distribution in machine windings," *IEEE Transactions on Energy Conversion*, vol. 4, no. 1, pp. 95–101, Mar. 1989, conference Name: IEEE Transactions on Energy Conversion.
- [30] D. Hanselman, "Brushless permanent magnet motor design," 2006, edition: 2nd ed. ISBN: 1881855155 Place: Lebanon, Ohio.
- [31] W. Hurley, E. Gath, and J. Breslin, "Optimizing the AC resistance of multilayer transformer windings with arbitrary current waveforms," *IEEE Transactions on Power Electronics*, vol. 15, no. 2, pp. 369–376, Mar. 2000, conference Name: IEEE Transactions on Power Electronics.
- [32] LWW, "TECHNICAL DATA FOR WINDING WIRE." [Online]. Available: https://www.retec.ch/index_htm_files/LWW_broschyr_20140508_LR.pdf
- [33] Henkel, "LOCTITE 435TM Technical Data Sheet," Dec. 2020. [Online]. Available: https://www.henkel-adhesives.com/pl/en/product/instant-adhesives/loctite_435.html
- [34] Honeywell, "Dielectric Constant Table." [Online]. Available: <https://prod-edam.honeywell.com/content/dam/honeywell-edam/pmt/hps/products/pmc/field-instruments/smartline-level-transmitters/smartline-guided-wave-level-transmitters/pmt-hps-dielectric-constant-table.pdf>
- [35] "AC/DC Module: Software for Simulating Static and Low-Frequency Electromagnetics." [Online]. Available: <https://www.comsol.com/acdc-module>
- [36] "Input Admittance Response of RLC Ladder Network with Mutual Coupling Between Multiple Coils - MATLAB & Simulink - MathWorks Nordic." [Online]. Available: <https://se.mathworks.com/help/physmod/sps/ug/mutualcoupling-multicoil.html>
- [37] "PSM3750 Frequency Response Analyzer," 2012. [Online]. Available: <https://www.newtons4th.com/products/frequency-response-analyzers/psm3750/>
- [38] "IAI2 Impedance Analyzer," 2012. [Online]. Available: <https://www.newtons4th.com/products/impedance-analysis-interface-2/>
- [39] H. Kolstad and K. Ljøekelsøy, *20 kW IGBT omformer. Beskrivelse*, 3rd ed. 7465 Trondheim: SINTEF ENergiforskning AS, Sep. 2002.
- [40] SEMIKRON, "SKM 400GB125D: Ultra Fast IGBT Modules," Jun. 2007. [Online]. Available: <https://docs.rs-online.com/fc64/0900766b81542a84.pdf>
- [41] Tektronix, "High Voltage Differential Probes," Oct. 2002. [Online]. Available: <https://docs.rs-online.com/6cd2/0900766b8032a746.pdf>
- [42] "FLUKE 80i-110s: AC/DC Current Probe," Oct. 2005. [Online]. Available: <https://docs.rs-online.com/3551/A700000008608015.pdf>
- [43] "RT-ZP03 User Manual," 2018. [Online]. Available: https://www.rohde-schwarz.com/no/search/download-center_63448.html?term=rtzp03
- [44] R. . Schwarz, "R&S@RTB2000 Oscilloscope," Feb. 2019. [Online]. Available: <https://docs.rs-online.com/4d50/0900766b816ff72d.pdf>
- [45] "WIMA MKP 10." [Online]. Available: https://www.mouser.com/datasheet/2/440/e_WIMA_MKP_10-1139811.pdf

APPENDIX A
WINDING CONFIGURATION



Fig. 21. The two turn winding



Fig. 22. The four turn winding

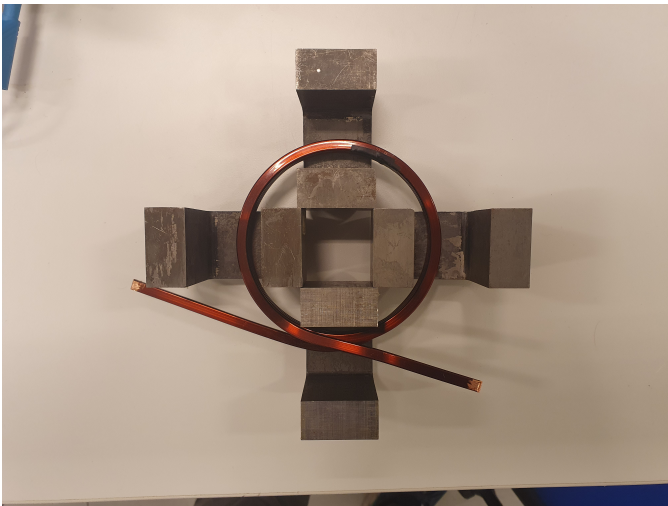


Fig. 23. The four turn winding with half the iron. There are placed four additional C-core on top of the four in the bottom.

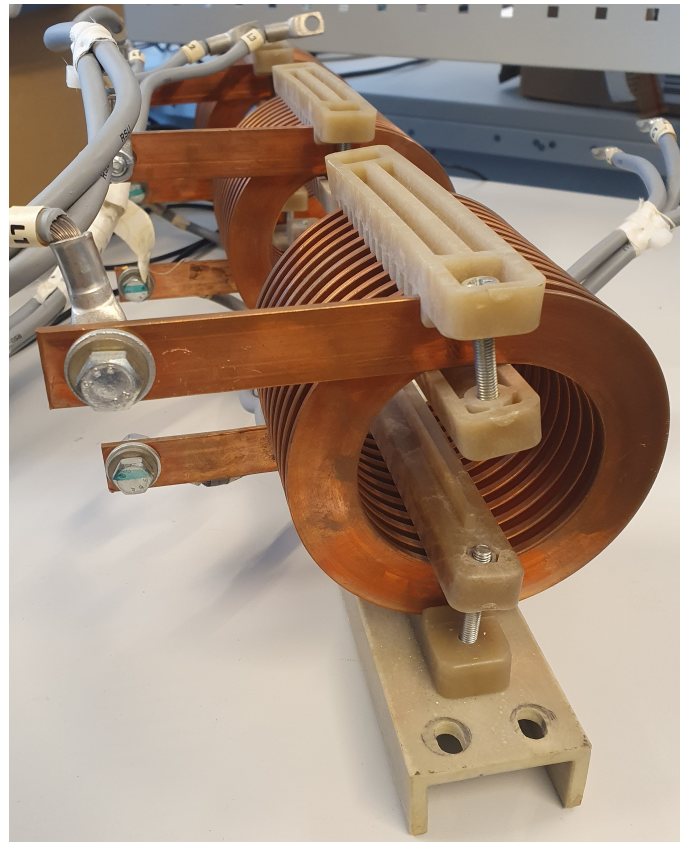


Fig. 24. The thirteen turn winding.

APPENDIX B
PROPOSED EQUIVALENT CIRCUITS

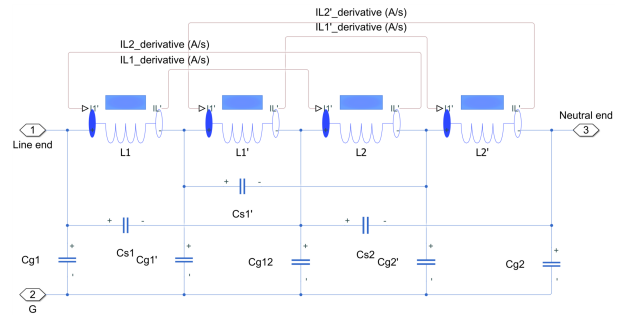
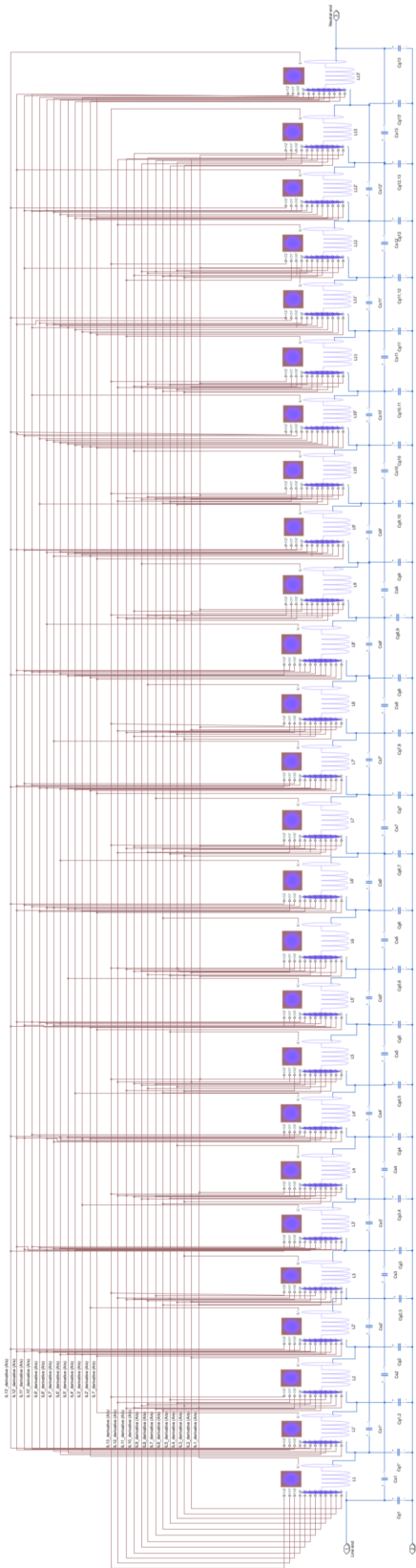


Fig. 25. Proposed equivalent model for simulation of two turn winding configuration in *Simulink*.

APPENDIX C
LINEARIZATION OF THE SIMULINK MODEL



```

1 %% Trim the Model
2 [t,x,y] = sim(modelFileName);
3 idx = find(t>simTime*0.1,1);
4 X = x(idx,:); % State value for linearization
5 U = y(idx); % Input value for linearization
6
7 %% Linearize the model
8 warnState = warning; % Store current warning...
9 warning('off','all'); % Turn off warnings
10 [A,B,C,D]=linmod(modelFileName,X,U);
11 warning(warnState); % Restore previous ...
12 % A, B, C, D are state space matrices
13
14 [A0,B0,C0,D0] = minreal(A,B,C,D); %Optionally
15
16 %% Plot the magnitude response
17 npts = 1e5;
18 f = logspace(1,10,npts);
19 G = zeros(1,npts);
20 G0 = zeros(1,npts);
21
22 for i=1:npts
23     G(i) = (C)*((2*pi*i*f(i)*eye(size(A))-A)...
24             ^-1)*B+(D);
25     G0(i) = (C0)*((2*pi*i*f(i)*eye(size(A0))-A0)...
26              ^-1)*B0+(D0);
27 end
28 Y = 1./G;
29 Y0 = 1./G0;
30 figure(1)
31 % Plot magnitude
32 ah(1) = subplot(2,1,1);
33 magline_h=loglog(f,abs(G),'b');
34 hold on
35 grid on
36 ylabel('Impedance [\Omega]');
37 title('Frequency Impedance Response');
38
39 % Plot phase
40 ah(2) = subplot(2,1,2);
41 phsline_h=semilogx(f,180/pi*unwrap(angle(G)),...
42                   'b');
43 hold on
44 grid on
45 ylabel('Phase [deg]');
46 xlabel('Frequency [Hz]');
47 % Create legend
48 legend('Simulated impedance response', '...
49         Location', 'southwest');

```

Fig. 26. Proposed equivalent model for simulation of thirteen turn winding configuration in *Simulink*.

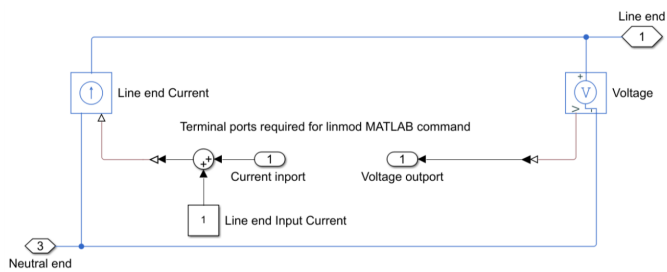


Fig. 27. The model used for the *MATLAB* command *linmod*.

APPENDIX D WATCHVIEW

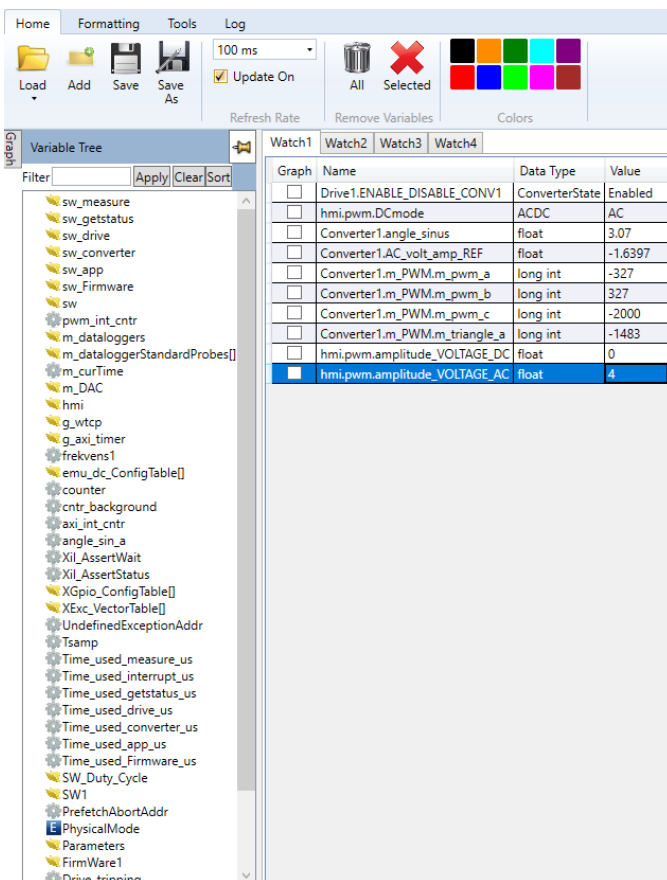


Fig. 28. The controlpanel in *WatchView*.

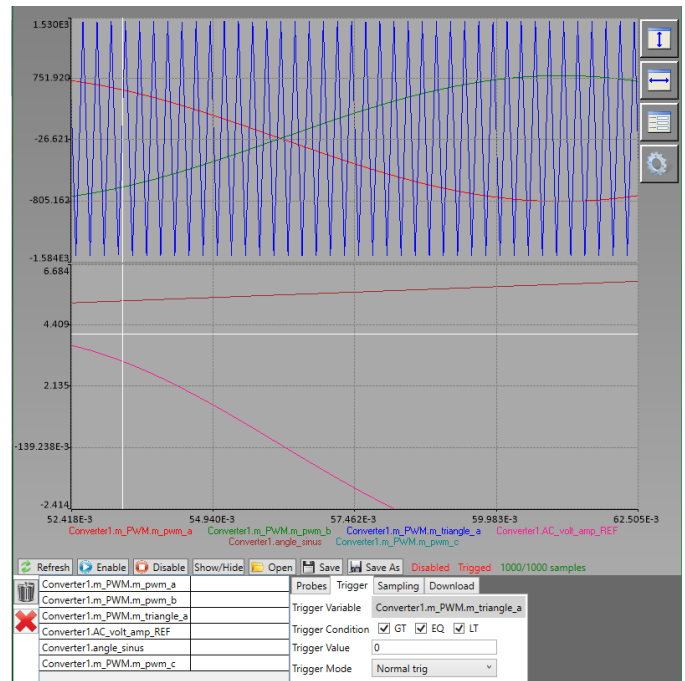


Fig. 29. The datalogger in *WatchView*.

APPENDIX E PARAMETERS

TABLE VIII
MUTUAL CAPACITANCE MATRIX IN PER UNIT LENGTH OF THE TWO TURN WINDING CONFIGURATION OBTAINED ANALYTICALLY AND WITH COMSOL.

Capacitance	2 turns [pF]	
	Analytical (10)	0.33
	294.47	0.33
COMSOL	6.15	316.48
	316.48	6.15

TABLE IX
MUTUAL CAPACITANCE MATRIX IN PER UNIT LENGTH OF THE FOUR TURN WINDING CONFIGURATION OBTAINED ANALYTICALLY AND WITH COMSOL.

Capacitance	4 turns [pF]			
	Analytical (10)	0.33	294.47	0
	294.47	0.16	294.47	0
	0	294.47	0.16	294.47
	0	0	294.47	0.33
COMSOL	5.11	311.72	3.09	3.61
	311.72	1.66	309.53	3.09
	3.09	309.53	1.66	311.72
	3.61	3.09	311.72	5.11

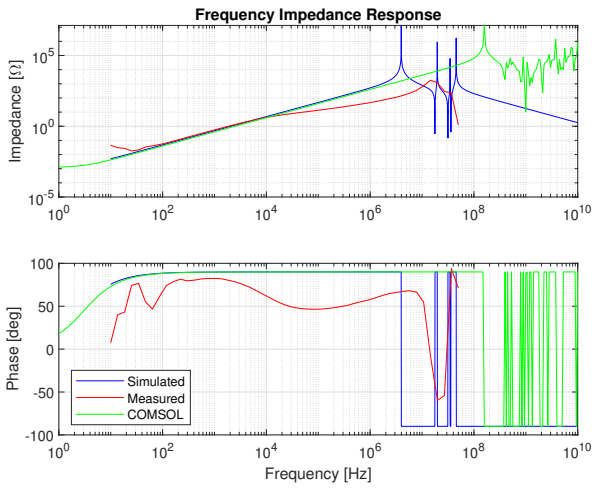


Fig. 32. Frequency impedance response of the four turn winding with iron.

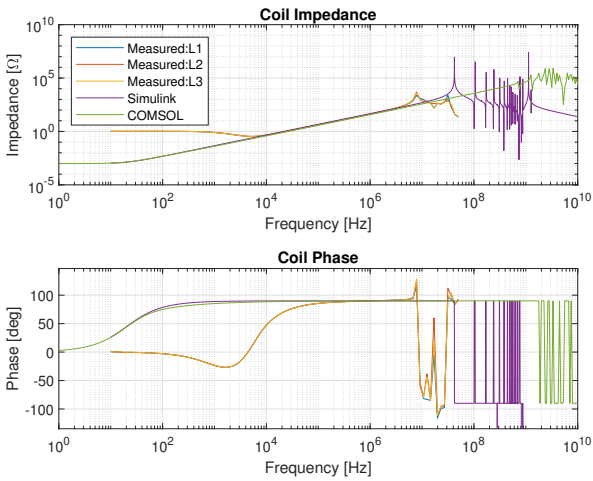
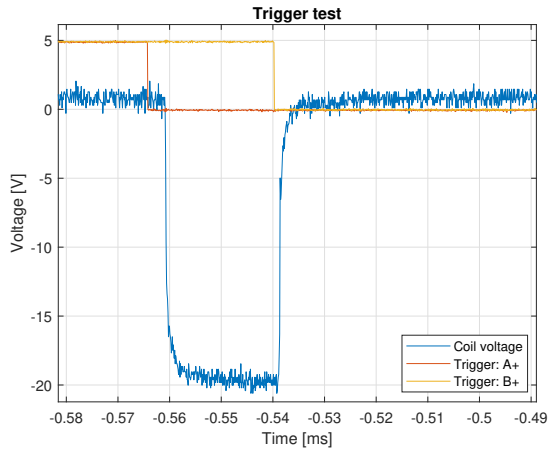


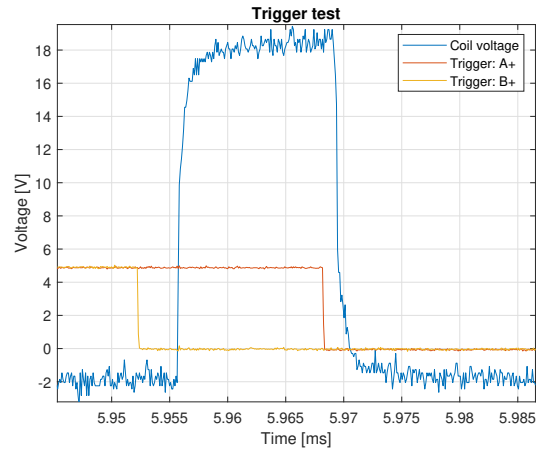
Fig. 33. Frequency impedance response of the thirteen turn winding: L1, L2 and L3 are the three different windings of the same design.

APPENDIX G

PWM INVERTER FED WINDING

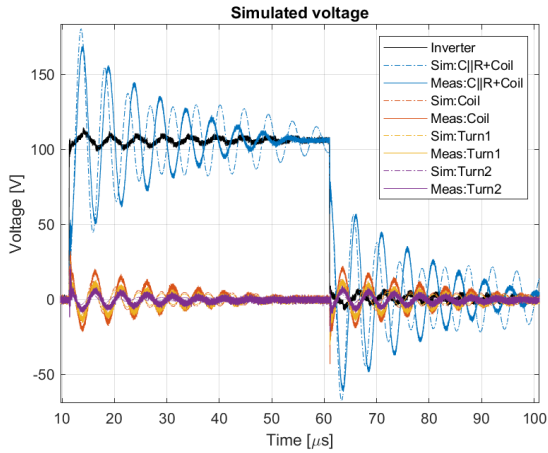


(a) Measured trigger signal for a square wave with negative amplitude.

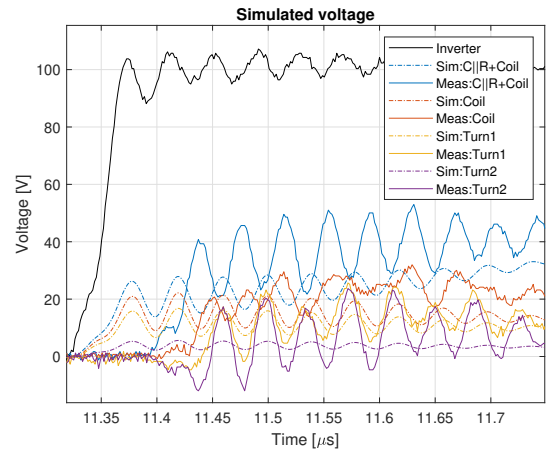


(b) Measured trigger signal for a square wave with positive amplitude.

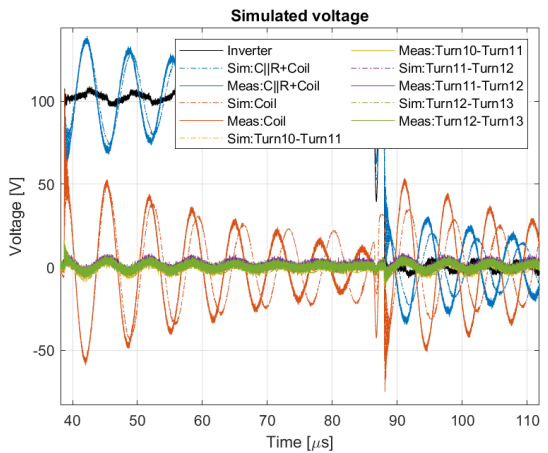
Fig. 34. Measured gate trigger signal for "+" transistors in phase leg A and B.



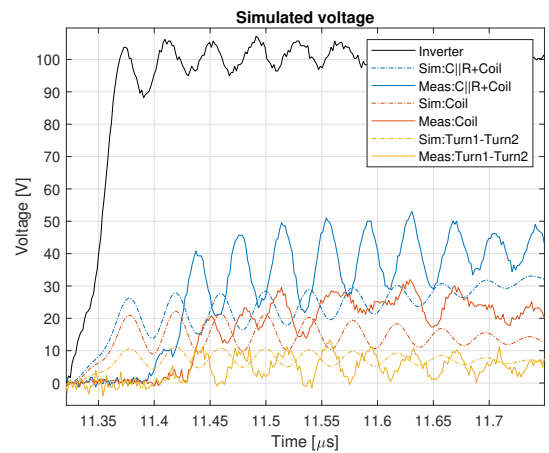
(a) Measured and simulated turn voltages in the two turn winding.



(b) Zoomed plot of the measured and simulated turn voltages in the two turn winding.

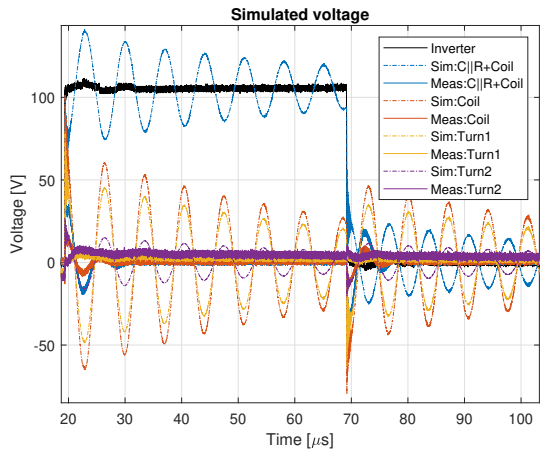


(c) Measured and simulated turn-to-turn voltages in the two turn winding.

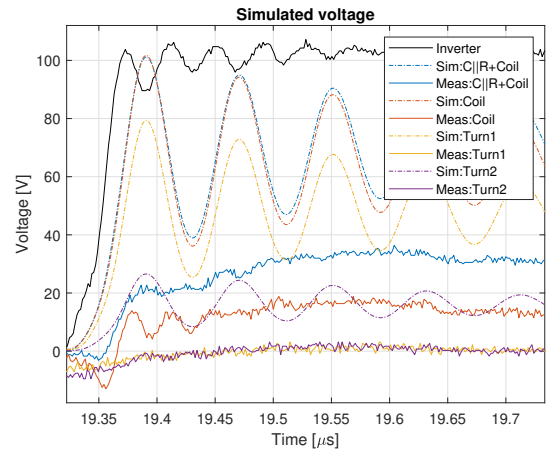


(d) Zoomed plot of the measured and simulated turn-to-turn voltages in the two turn winding.

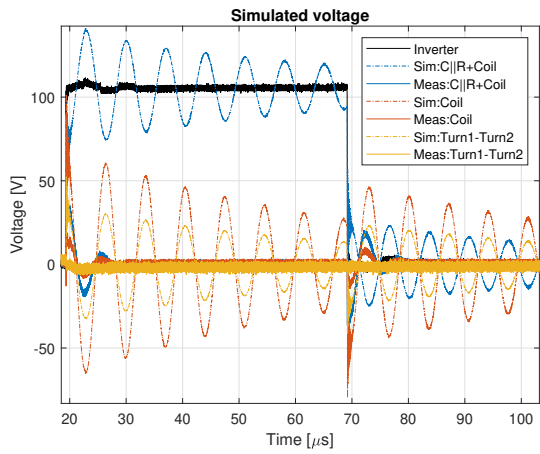
Fig. 35. Measured and simulated voltages in the two turn winding configuration without iron.



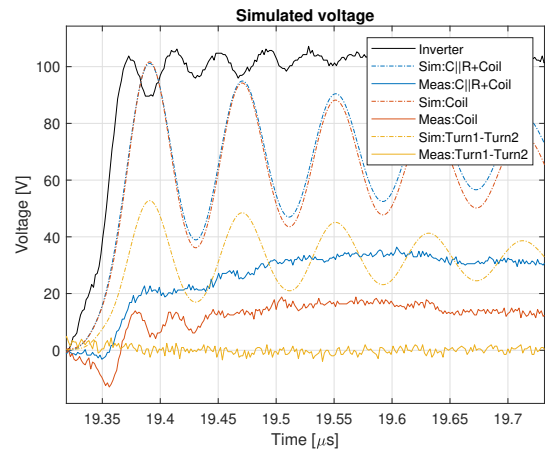
(a) Measured and simulated turn voltages in the two turn winding.



(b) Zoomed plot of the measured and simulated turn voltages in the two turn winding.

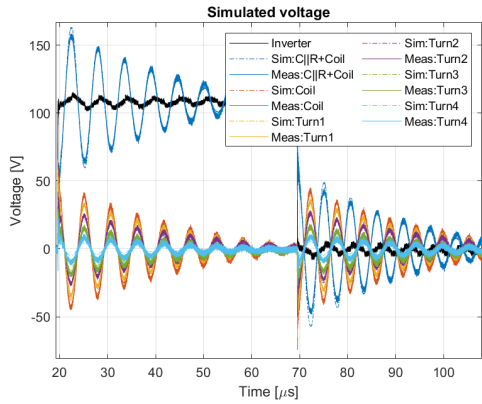


(c) Measured and simulated turn-to-turn voltages in the two turn winding.

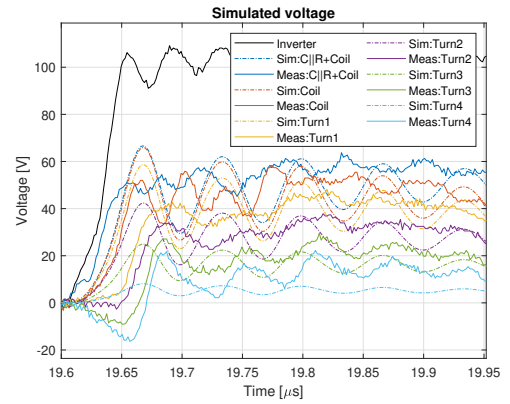


(d) Zoomed plot of the measured and simulated turn-to-turn voltages in the two turn winding.

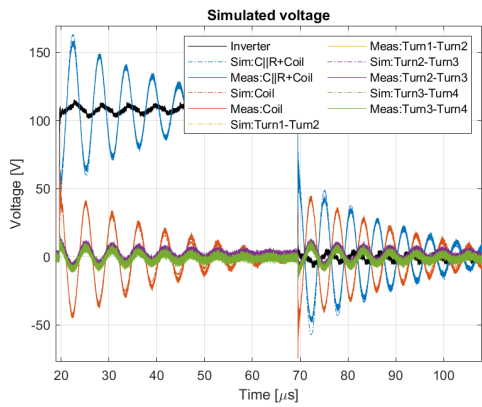
Fig. 36. Measured and simulated voltages in the two turn winding configuration with iron.



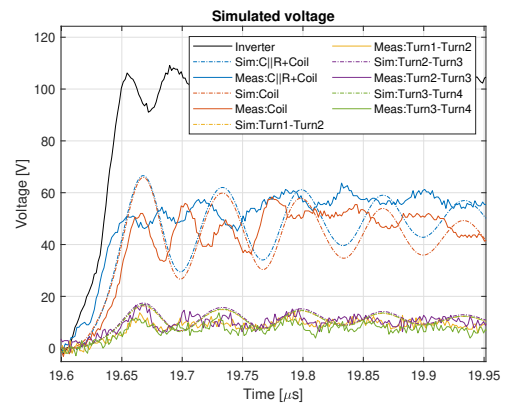
(a) Measured and simulated turn voltages in the four turn winding.



(b) Zoomed plot of the measured and simulated turn voltages in the four turn winding.

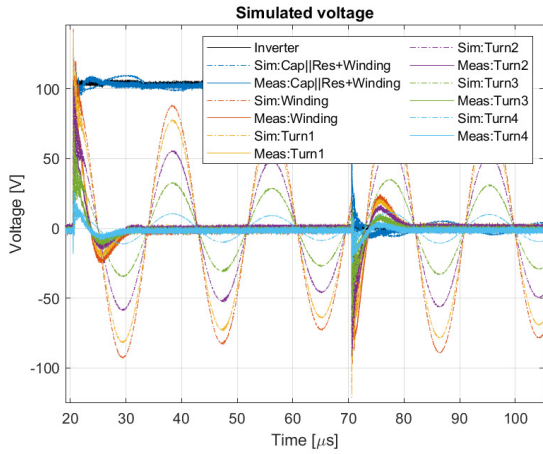


(c) Measured and simulated turn-to-turn voltages in the four turn winding.

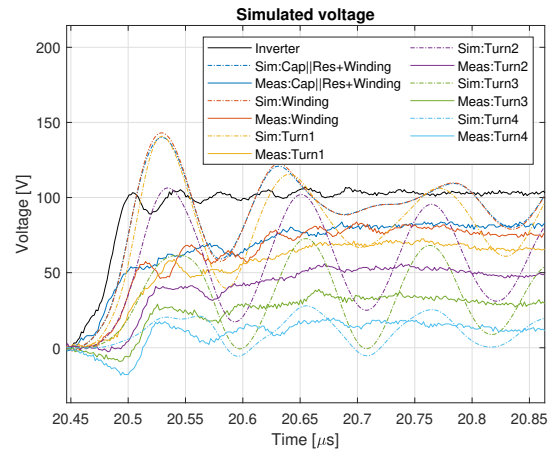


(d) Zoomed plot of the measured and simulated turn-to-turn voltages in the four turn winding.

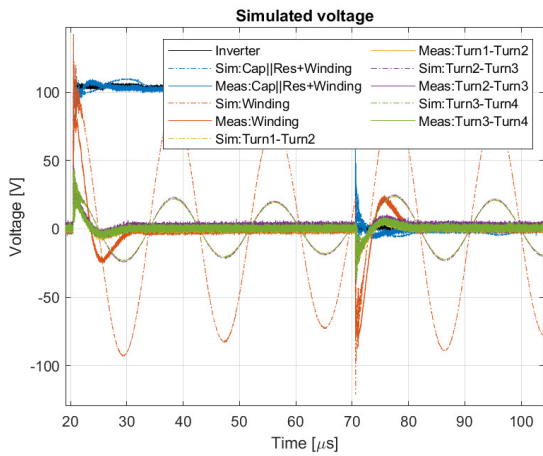
Fig. 37. Measured and simulated voltages in the four turn winding configuration without iron.



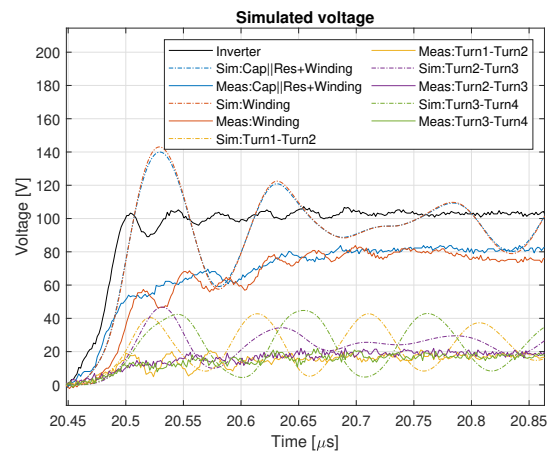
(a) Measured and simulated turn voltages in the four turn winding.



(b) Zoomed plot of the measured and simulated turn voltages in the four turn winding.

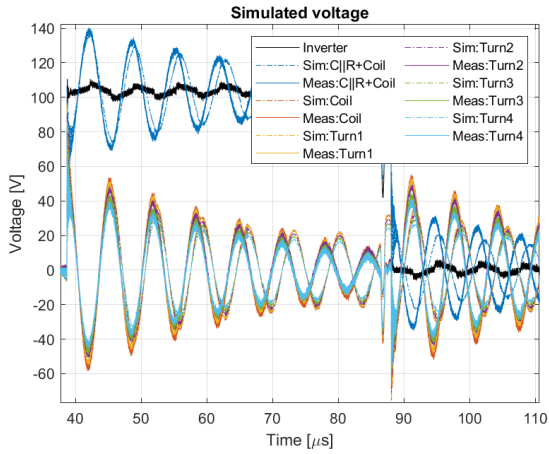


(c) Measured and simulated turn-to-turn voltages in the four turn winding.

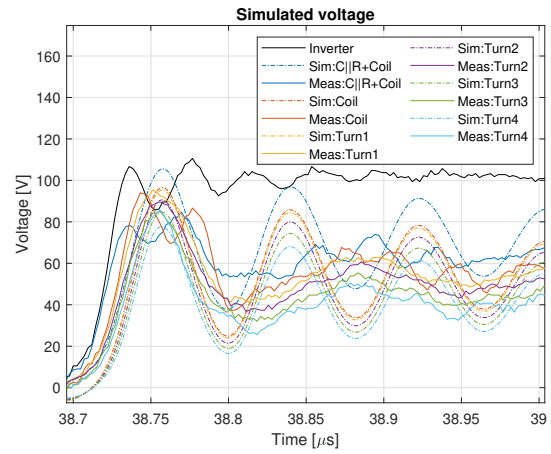


(d) Zoomed plot of the measured and simulated turn-to-turn voltages in the four turn winding.

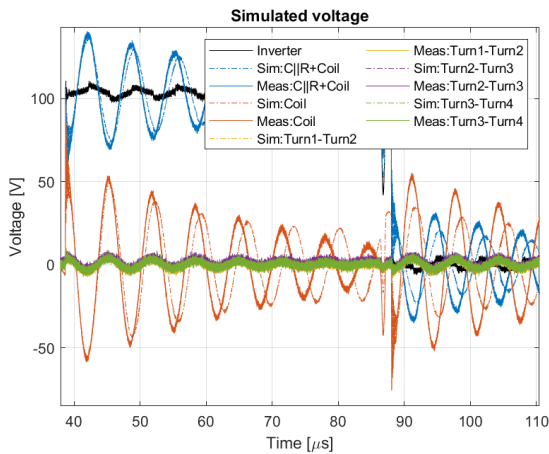
Fig. 38. Measured and simulated voltages in the four turn winding configuration with iron.



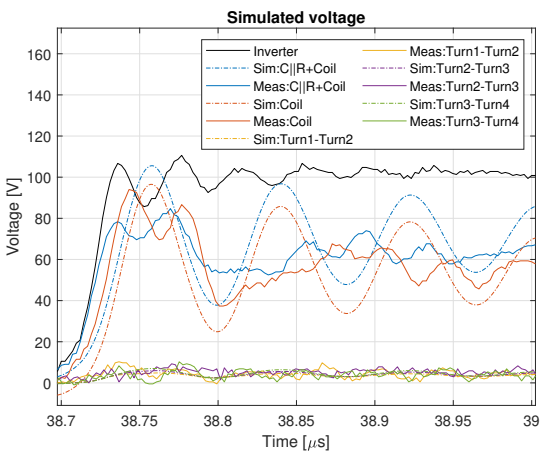
(a) Measured and simulated turn voltages for turn1 to turn4 of the thirteen turn winding.



(b) Zoomed plot of the measured and simulated turn voltages for turn1 to turn4 of the thirteen turn winding.

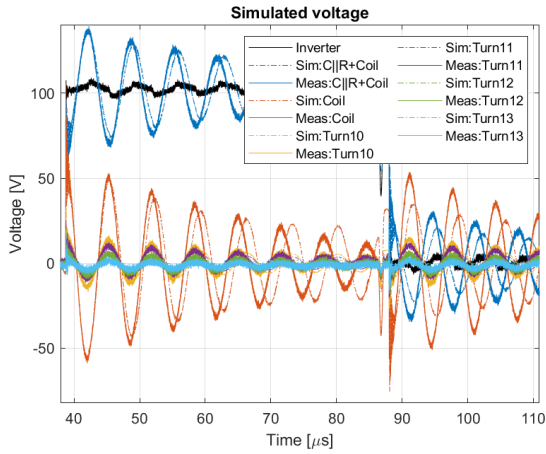


(c) Measured and simulated turn-to-turn voltages for turn1 to turn4 of the thirteen turn winding.

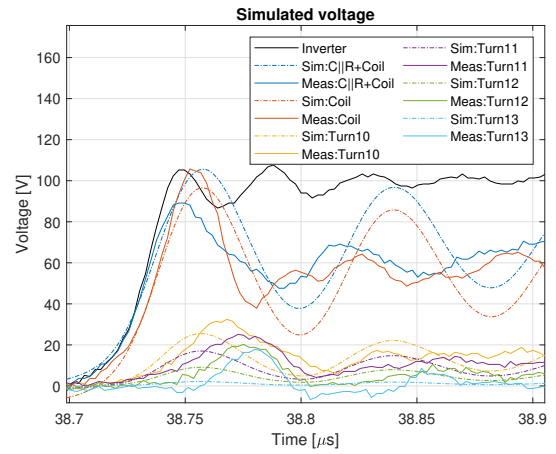


(d) Zoomed plot of the measured and simulated turn-to-turn voltages for turn1 to turn4 of the thirteen turn winding.

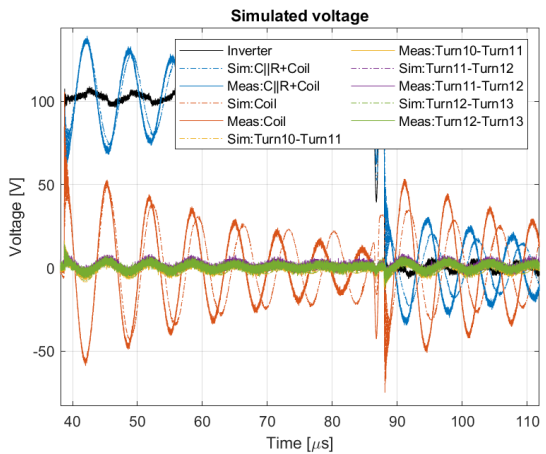
Fig. 39. Measured and simulated voltages for turn1 to turn4 in the thirteen turn winding configuration.



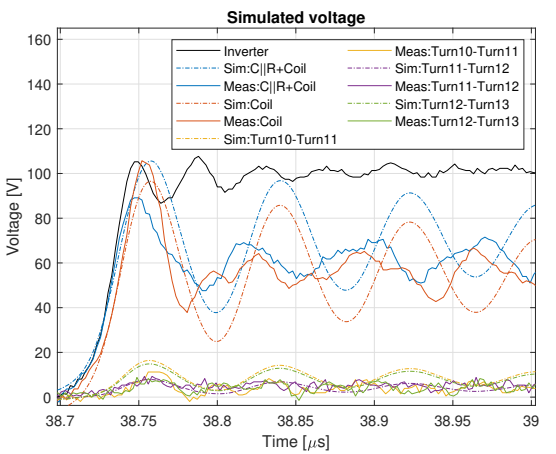
(a) Measured and simulated turn voltages for turn10 to turn13 of the thirteen turn winding.



(b) Zoomed plot of the measured and simulated turn voltages for turn10 to turn13 of the thirteen turn winding.



(c) Measured and simulated turn-to-turn voltages for turn10 to turn13 of the thirteen turn winding.



(d) Zoomed plot of the measured and simulated turn-to-turn voltages for turn10 to turn13 of the thirteen turn winding.

Fig. 40. Measured and simulated voltages for turn10 to turn13 in the thirteen turn winding configuration.

